ANNUAL REVIEWS

The Interstellar Dust Properties of Nearby Galaxies

Frédéric Galliano,[1,2] Maud Galametz,[1,2] and Anthony P. Jones[3]

[1]Institute of Research into the Fundamental Laws of the Universe (IRFU), Université Paris-Saclay, CEA, F-91191 Gif-sur-Yvette, France; email: frederic.galliano@cea.fr, maud.galametz@cea.fr

[2]Astrophysique, Instrumentation, Modélisation (AIM), CNRS UMR 7158, Université Paris-Diderot, Sorbonne Paris Cité, CEA, F-91191 Gif-sur-Yvette, France

[3]Institut d'Astrophysique Spatiale, CNRS UMR 8617, Université Paris-Sud and Université Paris-Saclay, F-91405 Orsay, France; email: anthony.jones@ias.u-psud.fr

ANNUAL REVIEWS CONNECT

www.annualreviews.org

- Download figures
- Navigate cited references
- Keyword search
- Explore related articles
- Share via email or social media

Keywords

ISM, dust, Magellanic clouds, nearby galaxies, methods

Abstract

This article gives an overview of the constitution, physical conditions, and observables of dust in the interstellar medium of nearby galaxies. We first review the macroscopic, spatial distribution of dust in these objects and its consequences for our ability to study grain physics. We also discuss the possibility of using dust tracers as diagnostic tools. We then survey the current understanding of the microscopic, intrinsic properties of dust in different environments, derived from different observables: emission, extinction, polarization, and depletions, over the whole electromagnetic spectrum. Finally, we summarize the clues about grain evolution, evidenced either on local scales or over cosmic time. We put in perspective the different evolution scenarios. We attempt a comprehensive presentation of the main observational constraints, analysis methods, and modeling frameworks of the distinct processes. We discuss neither the dust properties of the Milky Way and distant galaxies, nor circumstellar or active galactic nucleus torus dust.

Contents

1. INTRODUCTION

1.1. Interstellar Dust: A Key Galaxy Component

Interstellar grains are solid particles of size 0.3 nm $\lesssim r \lesssim$ 0.3 µm that are made of heavy elements (mainly O, C, Si, Mg, and Fe) available in the interstellar medium (ISM). They appear to be rather uniformly mixed with the gas in the ISM. Although accounting for $\lesssim$1% of ISM mass, they have a radical impact on galaxies, as they scatter and absorb starlight. In normal disk galaxies, they reradiate, in the infrared (IR) range, about 30% of stellar power, and up to 99% in ultraluminous IR galaxies (see, e.g., Clements et al. 1996). In addition, they are responsible for the heating of the gas in photodissociation regions (PDRs) by the photoelectric effect (PE) (Draine 1978). They are also catalysts of numerous chemical reactions, including the formation of the most abundant molecule in the Universe, H_2 (Gould & Salpeter 1963).

A detailed knowledge of grain properties (see the sidebar titled What Are the Dust Properties?) is crucial for studying the life cycle of the ISM and the evolution of galaxies, as it is needed to (*a*) unredden UV-visible observations, (*b*) study deeply embedded regions, (*c*) build reliable diagnostics of the physical conditions and of the evolutionary stage of a galaxy or a star-forming region, and (*d*) provide accurate prescriptions in photoionization and photodissociation models and in simulations of the star-formation process. However, as we show in this review, there remain several uncertainties about grain properties and their evolution. Dust physics is characterized by the great complexity of its object. The number of ways to combine elements to build interstellar solids is virtually limitless, and the manner of combination has consequences for the longevity of a particle and its observables. Progress in this field is thus mainly driven by empirical constraints: observations over the whole electromagnetic spectrum (**Figure 1**) and laboratory experiments on dust analogs.

WHAT ARE THE DUST PROPERTIES?

- **Dust mixture constitution.** The constitution of a grain mixture is defined by (*a*) the chemical composition of the bulk material and its stoichiometry; (*b*) the structure of the grains (crystalline, amorphous, porous, aggregated, etc.); (*c*) the presence of heterogeneous inclusions; (*d*) the presence of organic and/or icy mantles; (*e*) the shape of the grains; (*f*) the size distribution of the grains; and (*g*) the abundance of the grains relative to the gas.
- **Dust physical conditions.** A dust mixture with a given constitution can experience different physical conditions: (*a*) thermal excitation of the grains due to radiative heating (equilibrium or stochastic) or to collisional heating in a hot plasma; (*b*) grain charging by exchange of electrons with the gas; (*c*) alignment of elongated grains on the magnetic field; and/or (*d*) grain rotation (relevant for the smallest sizes).
- **Dust observables.** A grain mixture undergoing a given set of physical conditions will exhibit the following observables (represented in **Figure 1**): (*a*) emission [the emission of a thermal continuum (IR to millimeters) and of molecular and solid-state features (MIR), a possible microwave emission (centimeters), a possible luminescence (visible), and the possible polarization of the emission (IR to millimeters)]; (*b*) absorption [the absorption of light from a background source by a continuum, as well as by molecular and solid-state features, including diffuse interstellar bands and ices (X-ray to MIR); the possible polarization of this absorption (UV to visible)]; (*c*) scattering [the scattering of light from a bright source in our direction, as well as its polarization (X-ray to NIR)]; and (*d*) depletions (some elemental depletion patterns).

1.2. The Invaluable Laboratories of Nearby Galaxies

Most of our knowledge of dust properties comes from studies of the Milky Way (MW). However, as is demonstrated in this article, an increasing number of studies of nearby galaxies provide unique discriminating constraints on fundamental dust processes. Indeed, nearby galaxies harbor a wider diversity of environmental conditions (metallicity, star-formation activity, etc.) than can be found in the MW. In particular, they allow us to observe dust in extreme conditions. They also constitute a necessary intermediate step toward understanding distant galaxies, as they are spatially resolved and have better wavelength coverage. Another benefit of studying nearby galaxies is that, whereas interpretation can sometimes be difficult in the disk of the MW because we see the projected material of the entire disk, high-latitude observations of face-on galaxies can provide clearer sightlines.

We do not have a precise definition of nearby galaxies. They constitute a category expanding with the angular resolution of IR observatories. In this review, we consider them to be objects closer than ≃100 Mpc.

2. THE MACROSCOPIC DISTRIBUTION OF DUST IN GALAXIES

2.1. The Observational Point of View

Through mapping observations we can determine the spatial distribution of dust in galaxies, and with complementary spectroscopic observations we can also study the compositional variations of the dust across galaxies.

2.1.1. Dust distribution in disk galaxies. Dust biases our understanding of galactic structure, as it affects our derivation of luminosity profiles. The level of dust attenuation can strongly vary
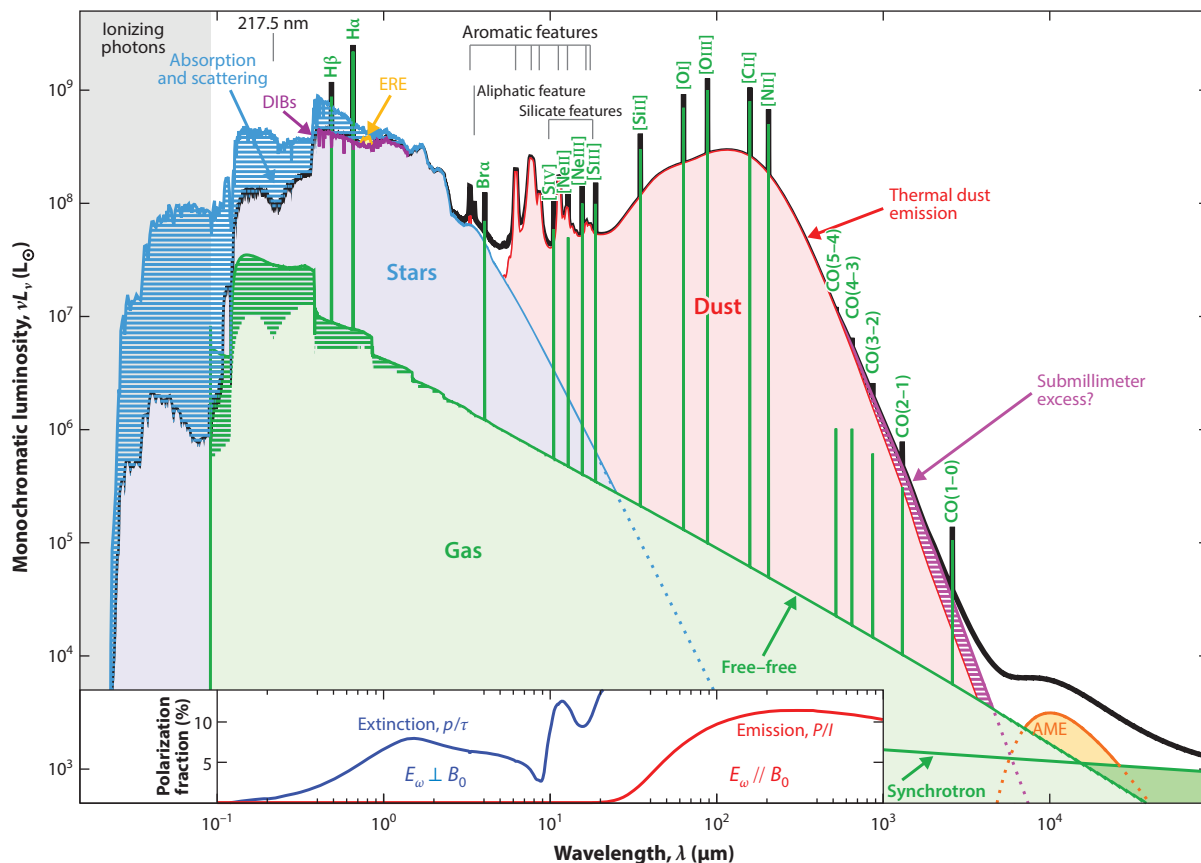
Figure 1

Spectral energy distribution of a typical late-type galaxy. The blue hatched area shows the power absorbed by dust. Typical diffuse interstellar band (DIB), extended red emission (ERE), and anomalous microwave emission (AME) spectra are shown, together with the most relevant gas lines. The free–free continuum is emitted by the deceleration of free electrons scattering off ions in ionized regions. The synchrotron continuum is emitted by electrons spiraling through the magnetic field. Here, ν is the radiation frequency and L_ν is the electromagnetic power emitted per unit frequency. (*Inset*) Model D of Guillet et al. (2018), with $G_0 = 100$; τ is the optical depth, p is the starlight polarization degree, P is the polarization intensity, I is the total intensity, E_ω is the light polarization vector, and B_0 is the magnetic field vector.

ISO: *Infrared Space Observatory* ($\lambda \simeq 5$–210 μm; 1995–98)

Scale length/height (*l*): the intensity at radius/azimuth r can be written as $I(r) \propto \exp(-r/l)$

depending on the sightline and from one galaxy to another (see, e.g., Calzetti 2001, Pierini et al. 2004, Battisti et al. 2016). Understanding how dust is distributed in galaxies is a necessary step to correct for these attenuation effects.

2.1.1.1. Mid-infrared scale length of dust. *Infrared Space Observatory* (ISO) observations helped assess the mid-IR (MIR) extent of nearby spirals (especially at 7 and 15 μm). They showed that MIR and optical emissions have very similar morphologies and concentration indices (Boselli et al. 2003). However, the MIR scale length tends to be systematically smaller than the optical (Malhotra et al. 1996), and the arm/interarm contrast is larger in MIR than in optical observations (Vogler et al. 2005). From a large range of morphologies, Roussel et al. (2001) also found that, whereas the IR-to-optical size ratio does not seem to be affected by the presence of a bar, this ratio is particularly reduced in HI-deficient galaxies and early-type galaxies (see also Bendo et al. 2002).

Numerous analyses have shown that the MIR disk has a similar scale length to those of $^{12}CO(1–0)$, Hα, and the radio continuum (Sauvage et al. 1996, Walsh et al. 2002, Vogler et al. 2005). The relation with Hα, in particular, indicates that the MIR scale length of a galaxy is determined by its star-forming activity. Indeed, MIR emission is enhanced in star-forming regions. With *Spitzer*, the improved sensitivity and spatial resolution opened a new frame to model the distribution of dust inside galaxies and, in particular, to derive radial profiles. *Spitzer* confirmed that the concentration index varies with the wavelength. Studying radial profiles of 75 nearby galaxies, Muñoz-Mateos et al. (2009b) found that the concentration indices drop in the unidentified infrared bands (UIBs) (5.8 and 8.0 μm; see Section 3.1.2). MIR observations at longer wavelengths indicate a wide variety of behaviors, including galaxies with very intense nuclear, circumnuclear, or outer-ring emissions and thus larger concentration indices (e.g., NGC 1291, NGC 1512, NGC 1097, NGC 3351).

Spitzer: *Spitzer Space Telescope* ($\lambda \simeq 3$–160 μm; 2003–9)

Concentration index: ratio between radii along the major axes encompassing 75% and 25% of the total flux of a galaxy

UIBs (unidentified infrared bands): prominent MIR features (**Figure 1**) attributed to carbonaceous grains (see Section 3.1.2)

Herschel: *Herschel Space Observatory* ($\lambda \simeq 55$–672 μm; 2009–13)

IRAS: *Infrared Astronomical Satellite* ($\lambda = 12$–100 μm; 1983)

COBE: *Cosmic Background Explorer* ($\lambda = 12$–5,000 μm; 1989–93)

2.1.1.2. Far-infrared/submillimeter scale length of dust. From ISO observations, it quickly became clear that the disk scale length of IR emission increases with the wavelength (Hippelein et al. 2003), with a far-IR (FIR) scale length being greater than an optical scale length (Tuffs et al. 1996, Alton et al. 1998, Haas et al. 1998, Davies et al. 1999, Trewhella et al. 2000). This FIR color gradient observed in the disk suggests that part of the FIR emission arises from grains heated by the radially decreasing diffuse interstellar radiation field (ISRF). In the edge-on spiral galaxy NGC 891, Popescu & Tuffs (2003) showed that intense FIR emission was associated with an extended H I disk, raising the question of whether grains are transported from the inner/optical disk, transferred via interactions or more resistant to destruction by shocks in the outer disk. *Spitzer*, *Herschel*, and plane- and ground-based submillimeter instruments have since revolutionized our vision of FIR/submillimeter emission and, in particular, have confirmed the detection of large, cold, extended disks (Block et al. 1994, Stevens et al. 2005, Hinz et al. 2012). In M51, the scale length of the 850-μm underlying exponential disk was estimated as $\simeq 5.5$ kpc (Meijerink et al. 2005). More statistically, Muñoz-Mateos et al. (2009a) and Hunt et al. (2015) examined the exponential dust profiles of 60–70 nearby galaxies. They showed that the FIR scale length does not vary strongly with galaxy type and is on average $\simeq 10\%$ larger than stellar scale lengths.

2.1.1.3. Scale-height studies. In the Galaxy, a scale height on the order of 100 pc was estimated using *Infrared Astronomical Satellite* (IRAS) observations at 100 μm, with a vertical distribution that correlates with the distribution of the H I gas (Boulanger & Perault 1988). Davies et al. (1997) extended the analysis to the colder dust phase using *Cosmic Background Explorer* (COBE) data and found a more diffuse 20-K dust component, with a cold dust scale height of $\simeq 500$ pc. Outside the MW, edge-on galaxies are ideal objects to constrain this parameter. Xilouris et al. (1999) studied the stellar and dust disks in five of these edge-on late-type spirals and found that their mean optical-to-dust scale-height ratio was $\simeq 1.8$. This ratio is often used as an a priori assumption for disk models (Tempel et al. 2010). Quantifying the dust scale height is undoubtedly more difficult for face-on galaxies. Padoan et al. (2001) proposed a new method to measure the average scale height in face-on disk galaxies. Using H I data in the Large Magellanic Cloud (LMC), they interpreted the break in the power-law shape of the spectral correlation function as the boundary of the gas mass distribution and velocity field. This method has been since then applied to derive scale-height estimates of the warm and cold dust. In the LMC, Block et al. (2010) found that the break in the power spectrum occurs on scales of $\simeq 100$–200 pc in the FIR. Combes et al. (2012) found similar scale heights in M33. This technique is limited by the resolution of the observations: Artificial breaks can appear when the scale height is too close to the resolution scale. Finally, radiative transfer codes are robust tools to model the absorption and reemission by dust and to derive structural parameters (see Section 2.2). The model of Baes et al. (2003), for instance,

has been used to derive scale lengths and scale heights in edge-on galaxies (De Looze et al. 2012a, De Geyter et al. 2015, Viaene et al. 2015). The scale heights derived in these studies typically range from $\simeq 100$ to 200 pc.

2.1.2. Dust distribution in irregular galaxies. Irregular galaxies can contain large amounts of atomic gas that typically extends to twice their Holmberg radius (see, e.g., Huchtmeier et al. 1981). They are also rich in dust, with very similar optical and MIR scale lengths (Hunter et al. 2006). The dust emission in irregular galaxies is clumpy and warm, with a hot dust and UIB emission mostly observed toward bright HII regions. This suggests that massive stars are a major source of heating in these environments (see, e.g., Hunter et al. 2006).

2.1.3. Dust distribution in dwarf galaxies. One of the main characteristics of dwarf galaxies is their low metallicity (Z). As we discuss in Section 4.3.2, the dust-to-gas ratio scales roughly with Z. The ISM in these objects is less dusty and thus more transparent. As is true in irregular galaxies, massive stars are a major source of heating in these objects (see, e.g., Walter et al. 2007), and they are permeated by supernova (SN)-triggered shock waves (see, e.g., Oey 1996). Finally, these galaxies exhibit large HI envelopes. The IR-emitting region can correspond to only $\simeq 20$–30% of the total mass of the system (Walter et al. 2007).

2.1.4. Dust distribution in elliptical galaxies. Elliptical galaxies possess very little dust: The average dust-to-stellar mass ratio is $\simeq 50$ times lower than that of spiral galaxies (Smith et al. 2012). Dust lanes are, however, commonly detected in elliptical galaxies (Sadler & Gerhard 1985). Jura et al. (1987), for instance, found that half of nearby ellipticals are detected at IRAS wavelengths. Smith et al. (2012) found that the elliptical galaxies detected at 250 µm tend to have higher X-ray luminosities. Their dust may be heated in part by electron collisions (Goudfrooij & de Jong 1995).

2.1.5. Dust distribution in galactic superwinds. Dust at high latitudes or in galactic halos can be explained as resulting from various mechanisms, including stellar feedback, transport via cosmic ray–driven winds, and radiation pressure on the grains (Bocchio et al. 2016). The last mechanism could also partly contribute to driving the galactic superwinds in star-forming galaxies, although several studies have shown that it is insufficient as the only mechanism (Hopkins et al. 2012, Contursi et al. 2013). Contursi et al. (2013) showed that, in the outflow of M82, dust is slower than the ionized and molecular gas, indicating that dust grains are kinematically decoupled from the gas in the superwind. Most of this dust is not fast enough to escape and may fall back into the galaxy disk.

2.1.6. Dust heating sources probed with infrared colors. Dust emits in the IR–submillimeter range. In this regime, the ratio of two fluxes (or color) provides information on the grains in the same way that optical colors provide information on the stars. These colors are widely used to understand the sources of heating of ISM dust. From IRAS observations, Lonsdale Persson & Helou (1987) were among the first to use the correlation of the $L_\nu(60)/L_\nu(100)$ color temperature with tracers of old stars to study their heating contribution. With *Spitzer* observations, global $L_\nu(8)/L_\nu(160)$ ratios were then used to probe the origin of the UIBs (see Section 3.1.2) and to show that their emission correlates surprisingly well with that of the diffuse, cold dust (see, e.g., Bendo et al. 2008). Resolved observations later showed that enhancements in the $L_\nu(8)/L_\nu(160)$ ratio are spatially offset relative to the star forming-regions, suggesting that the UIBs could be partly excited by photons leaking out of star-forming regions (Jones et al. 2015) by up to 30–40% (Crocker et al. 2013).

With the arrival of *Herschel*, studies pushed toward longer wavelengths, tracing dust at lower temperatures. *Herschel* ratios have been extensively correlated with both stellar surface brightnesses and star-formation rate tracers. These analyses usually find a strong correlation of the $L_\nu(250)/L_\nu(350)$ and $L_\nu(350)/L_\nu(500)$ ratios with the local stellar mass, showing the importance of the lower-mass stellar populations as a heating source of the coldest dust population (Bendo et al. 2010, Boquien et al. 2011). By correlating the submillimeter ratios with a linear combination of tracers of the total stellar population (1.6 μm) and of the star-forming regions (Hα), Bendo et al. (2012) segregated the two different heating sources and found that, in disk galaxies, $\simeq$60–90% of the heating of cold dust is dominated by lower-mass stars. Ratios at shorter wavelengths, such as $L_\nu(70)/L_\nu(160)$ and $L_\nu(160)/L_\nu(250)$, are less correlated with radius and more strongly correlated with the star-formation rate (SFR). Boselli et al. (2010) and Boquien et al. (2011) found similar results, showing in particular that the warm dust temperature, measured by the $L_\nu(60)/L_\nu(100)$ ratio, seems to increase with the birth rate parameter, b, whereas the cold dust temperature, measured by the $L_\nu(350)/L_\nu(500)$ ratio, seems to be anticorrelated with b. However, the old stellar population probably continues to also play a role in the heating of the warm dust, with a contribution that seems to correlate with the evolutionary stage of the galaxy (for instance, there is a significant global contribution of bulge stars in early-type galaxies, such as M81; Bendo et al. 2012). In contrast, Rémy-Ruyer et al. (2013) showed a trend of color temperature with metallicity, suggesting that low-Z systems are, on average, hotter (see also Melisse & Israel 1994). This is conjectured to result from the enhanced contribution of young star heating at low Z.

New results from radiative transfer models (see Section 2.2) are now quantifying better the respective contributions of the different stellar populations to dust heating. In M31, it was shown that 90% of dust could be heated by the lower-mass stellar populations (Viaene et al. 2017, figure 8). Further detailed analysis would be necessary to quantify more robustly the contribution as a function of the galaxy type.

2.2. The Radiative Transfer Approach

The observed properties discussed in Section 2.1 can be investigated more comprehensively by modeling the effects of dust extinction and emission.

2.2.1. Radiative transfer models. The most rigorous way to understand the effects of dust extinction and emission on ultraviolet (UV)-to-millimeter observations of galaxies is to model the radiative transfer (RT) of the starlight through their dusty ISM in a realistic three-dimensional (3D) geometry. Several teams have developed such code for disk galaxies (see, e.g., Baes et al. 2003, Bianchi 2008, Popescu et al. 2011). Such code solves the RT equation, accounting for multiple anisotropic scatterings, absorption, and dust and stellar emission. This type of computation is numerically intensive. Most models implement a Monte Carlo method, with various refinements and heavy parallelization.

2.2.2. Application to galaxies. Applying 3D RT models to reproduce the spatial flux distribution of galaxies, in all wavebands, is not straightforward. Indeed, the observations provide only 2D projected constraints. This is why most studies favor edge-on galaxies, as the images of such objects provide constraints on both the radial and azimuthal distributions, assuming axisymmetry (**Figure 2**). Several teams have studied the effect of extinction on the optical data of disk galaxies using such models (see, e.g., Xilouris et al. 1999, Alton et al. 2004, Bianchi 2007). They were able to answer the recurring question about the optical thickness of disk galaxies (Disney et al. 1989). In particular, Xilouris et al. (1999) found that the face-on optical depth of typical spiral galaxies is
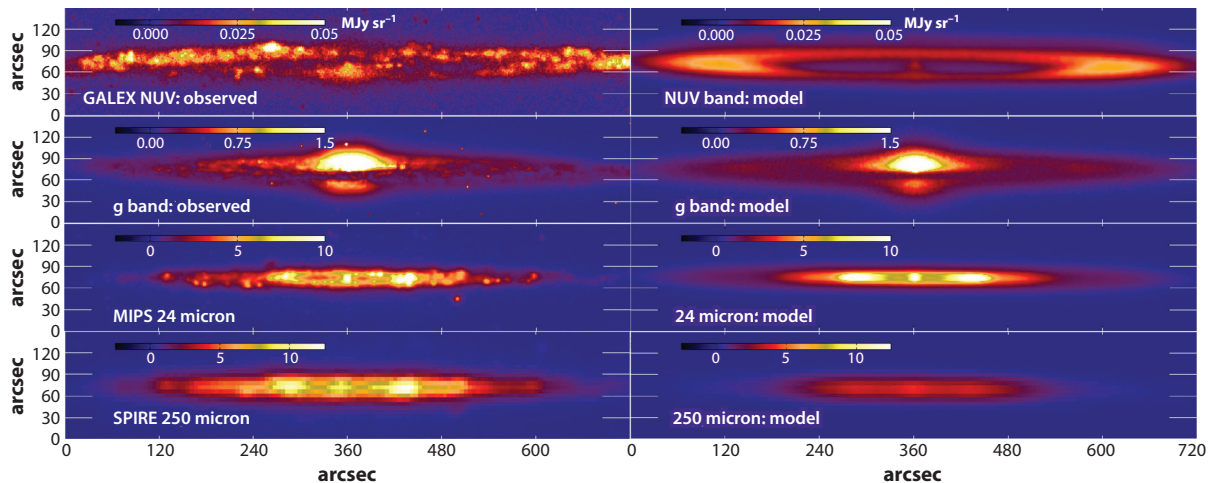
Figure 2

Radiative transfer model of NGC 4565 (De Looze et al. 2012a). Observations (*left*) are compared to model results (*right*). This galaxy is shown through the near-UV (NUV) *Galaxy Evolution Explorer* (GALEX) band, the g band (464 μm), the Multiband Imaging Photometer (MIPS) onboard *Spitzer* 24-μm band, and the Spectral and Photometric Imaging Receiver (SPIRE) onboard *Herschel* 250-μm band.

less than one in all optical bands. These studies also provide more comprehensive results on the nature of the dust's heating sources and on the scale length and scale height (see Sections 2.1.6 and 2.1.1.3). Finally, these models account for the energy balance between the escaping UV–visible light and the reemitted IR–submillimeter radiation. Interestingly, several studies report a deficit of modelled FIR emission by a factor $\simeq 3$–4 compared to observations (Alton et al. 2000, 2004; Dasyra et al. 2005; De Looze et al. 2012a,b). This discrepancy is thought to result from a lack of detail in modeling the geometry. In particular, the presence of young stars, deeply embedded in molecular clouds, could compensate for this deficit without significantly altering the extinction (see, e.g., Baes et al. 2010).

2.3. Phenomenological Spectral Energy Distribution Modeling

RT is impractical in most cases, as the geometry of the source is often poorly known.

2.3.1. The mixing of physical conditions. RT models of whole galaxies do not resolve sufficiently small spatial scales (Equation 2; see the sidebar titled What Are the Spatial Scales Relevant to Dust Heating?). Hence, we are usually compelled to make approximations regarding the complex topology of the studied object.

Monochromatic luminosity: $L_\nu(\lambda)$, the power emitted per unit frequency ($L_\odot$/Hz) at wavelength λ (μm)

2.3.1.1. The isothermal approximation. To first order, one can ignore the variations of the physical conditions. The modified blackbody (MBB) approximation, the most widely used approximation, assumes that IR emission comes from identical grains at a single temperature, $T_{\rm dust}$, with a power-law, wavelength-dependent, dust mass absorption coefficient, or opacity:

$$\underbrace{L_\nu(\lambda)}_{\text{monochromatic luminosity}} = \underbrace{M_{\rm dust}}_{\text{dust mass}} \times \underbrace{\kappa(\lambda_0) \cdot (\lambda_0/\lambda)^\beta}_{\text{parametric opacity}} \times \underbrace{4\pi B_\nu(\lambda, T_{\rm dust})}_{\text{blackbody}}, \qquad 1.$$

WHAT ARE THE SPATIAL SCALES RELEVANT TO DUST HEATING?

The physical condition of dust varies on spatial scales on the order of the mean free path of a V-band photon:

$$l_V = \left[\underbrace{\overbrace{Y_{\text{dust}}}^{\text{dust-to-H mass ratio}} \times \overbrace{m_H}^{\text{mass of an H}} \times \overbrace{n_H}^{\text{density}}}_{\text{dust mass per unit ISM volume}} \times \underbrace{\kappa(V)}_{\text{dust opacity}} \right]^{-1} \simeq \frac{600 \text{ pc cm}^{-3}}{n_H}. \qquad 2.$$

For a diffuse region ($n_H \simeq 10 \text{ cm}^{-3}$), $l_V \simeq 60$ pc, whereas for a dense region ($n_H \simeq 10^4 \text{ cm}^{-3}$), $l_V \simeq 0.06$ pc. Thus, to resolve dust temperature variations, in an edge-on cloud, we would need to resolve structures of $\simeq 0.06$ pc, which translates into $\simeq 0.2$ arcsec for the LMC [a typical resolution for the Atacama Large Millimeter Array (ALMA) and the *James Webb Space Telescope* (JWST)] and $\simeq 0.01$ arcsec for M31 (currently inaccessible). For a face-on cloud, there will be mixing along the line of sight, in any case.

where B_ν is the Planck function. In principle, a fit of this model, varying M_{dust}, T_{dust}, and β (the emissivity index), provides constraints both on the grain physical conditions (through T_{dust}) and on their composition (through β). Indeed, different materials can have different values of β. An inverse relation between T_{dust} and β is also observed in some laboratory analogs (see, e.g., Mennella et al. 1998, Boudet et al. 2005). However, a gradient of temperature tends to broaden the spectral energy distribution (SED). The inherent mixing of physical conditions is thus enough to bias these estimates (see, e.g., Juvela & Ysard 2012, Hunt et al. 2015). In addition, the contribution from out-of-equilibrium grains can be non-negligible at $\lambda \lesssim 70$ μm (**Figure 3a**; for detail on the various dust heating regimes, see the sidebar titled Dust Heating Regimes: Equilibrium or Stochastic?). In this sense, MBB-derived parameters are ambiguous effective quantities (T_{eff}, β_{eff}) that can be reliably interpreted only in terms of intrinsic grain properties: (*a*) in diffuse regions, where the ISRF is expected to be roughly uniform, or in cold cores; and (*b*) provided that the fit is constrained at sufficiently long wavelengths ($\lambda \gtrsim 100$ μm).

Alternatively, one can fit an observed SED with a full dust mixture (as in **Figure 3a**), varying the ISRF intensity, U, and the mass of each subcomponent (**Figure 3b**). With such an approach, the MIR wavelengths can be interpreted in terms of size distribution variations provided that the ISRF is roughly uniform.

2.3.1.2. Distributions of starlight intensities. It is possible to empirically account for the mixing of physical conditions by parameterizing the ISRF intensity distribution. One of the most useful prescriptions is given by Dale et al. (2001). It assumes that the dust mass in different bins of U follows a power law: $dM_{\text{dust}} \propto U^{-\alpha} dU$ for $U_{\min} < U < U_{\max}$. This way, varying the parameters $U_{\min}$, $U_{\max}$, and α, an observed SED can be fit with a combination of physical conditions. This is demonstrated in **Figure 3c**. One of the limitations of this approach is that it ignores the variation of the grain properties with environments. As is discussed in Section 4.2, the carriers of the UIBs are usually destroyed in regions of high U. FIR emissivity will also change because of mantle processing and evaporation (see Section 4.2.1). In addition, there is a degeneracy between the ISRF distribution and the fraction of small grains. This is demonstrated in **Figure 3b,c**. The same SED is fitted either with an isothermal model, accounting for the MIR fluxes by raising the fraction of small grains (**Figure 3b**), or by adding hotter regions (**Figure 3c**). Fortunately, the dust mass is dominated by the coldest large grains and can thus be reasonably derived with this type of model. This type of model is superior to MBB, as the latter underestimates the mass by

ISRF intensity (U): integrated in [0.0912, 8] μm; it is normalized so that $U = 1$ in the Solar Neighborhood

a Heating regimes   **b** Free size distribution   **c** Free ISRF distribution
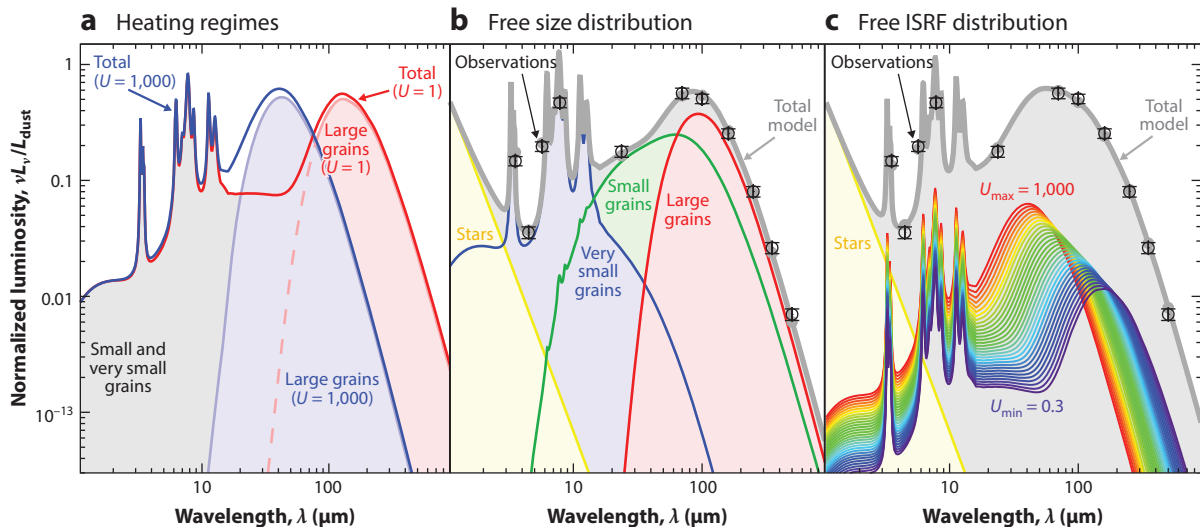
Figure 3

Phenomenological spectral energy distribution (SED) modeling. (*a*) Dust emission model of the Milky Way (Jones et al. 2017), heated by the interstellar radiation field (ISRF) of the diffuse interstellar medium (ISRF intensity $U = 1$; *red*) and higher ($U = 1,000$; *blue*). This demonstrates that the shape of the SED of small, out-of-equilibrium grains (*gray shading*) is independent of U. By contrast, the shape of the SED of large grains, which are at equilibrium with the ISRF, shifts to shorter wavelengths when U increases, as their equilibrium temperature increases. (*b*) Simulated broadband observations (*black*) fitted by varying the mass fractions of very small ($0.35 \leq r < 1.5$ nm; *blue*), small ($1.5 \leq r < 20$ nm; *green*) and large ($0.02 \leq r < 0.3$ μm; *red*) grains, with a single $U = 8$ (fitted). (*c*) The same simulated observations as in panel *b*, alternatively fitted with a starlight intensity distribution ($\propto U^{-\alpha}$; *rainbow colors*).

≃30% in rather diffuse regions and by a factor as great as ≃3 in regions where there is a lot of mixing (e.g., Galliano et al. 2011, Galametz et al. 2012, Rémy-Ruyer et al. 2015).

More complex parameterizations of the ISRF distribution are possible (see, e.g., Draine & Li 2007). It is also possible to build multicomponent models in which the phase composition is linked to the star-formation history (see, e.g., da Cunha et al. 2008).

2.3.1.3. A matryoshka effect. A consequence of the mixing of physical conditions is that the derived dust mass depends on the spatial resolution. Indeed, cold regions have a weak luminosity but can be massive. When a large region is integrated, the cold components can be hidden,

---

DUST HEATING REGIMES: EQUILIBRIUM OR STOCHASTIC?

- **Thermal equilibrium.** The enthalpy, H, of grains with large enough radii ($r \gtrsim 0.02$ μm) is, in most cases, significantly higher than the mean energy of the incident photons they absorb, $\langle h\nu \rangle \ll H$. Therefore, a single photon event does not notably modify their temperature. They are at equilibrium with the radiation field. Their spectrum is proportional to a Planck function times a wavelength-dependent opacity (**Figure 3a**).
- **Stochastic heating.** By contrast, for small grains ($r \lesssim 0.02$ μm), $\langle h\nu \rangle \gtrsim H$. A single photon event will cause temperature spikes at a few hundred degrees Kelvin (depending on its size), followed by a significant cooling before the next absorption (Draine & Anderson 1985). These temperature fluctuations result in a broad spectrum, extending down to the MIR range (**Figure 3a**). Such grains are out of thermal equilibrium.

whereas they can be accounted for in smaller-resolution elements. In practice, the derived dust mass is always higher (by up to $\simeq 50\%$), when estimated at high spatial resolution, than when using integrated fluxes (Galliano et al. 2011, Galametz et al. 2012, Roman-Duval et al. 2014). The estimate at high resolution is thought to be more accurate. This result depends on the environment, on the maximum resolution, and on the parameterization of the ISRF distribution. It is not always seen (e.g., Aniano et al. 2012).

2.3.2. Fitting methodologies. SED fitting is a technical matter. First, the contribution to the broadband fluxes of several non-dust-related processes need to be subtracted, or at least accounted for in the uncertainties (**Figure 1**): (*a*) the free–free and synchrotron radio continua; (*b*) ionic, PDR, and molecular lines; (*c*) foreground Galactic and zodiacal emission; and (*d*) background galaxies. Second, finding the best model parameters is not straightforward. The least-squares method is the most widely used approach to fit an SED model to IR observations. However, Shetty et al. (2009) have shown that this approach leads to a noise-induced false anticorrelation between T_{dust} and β in the case of a MBB. It makes the determination of the possible real relation between T_{dust} and β (see Section 2.3.1.1) difficult. Galliano (2018) showed that similar noise-induced correlations are found between most parameters when using full dust models with an ISRF distribution.

Bayesian inference is becoming increasingly popular with the development of powerful computers. Several SED models implement it to provide rigorous uncertainty estimates of the derived parameters. However, Galliano (2018) has shown that this approach is not sufficient to resolve the problem of noise-induced correlations. In fact, Kelly et al. (2012) have demonstrated, in the case of a MBB, that it is necessary to use the more complex hierarchical Bayesian inference to achieve this goal. Galliano (2018) has extended this technique to full dust models with ISRF distributions and has shown that it leads to significant improvements in the recovery of the dust parameters and of their intrinsic correlations.

2.4. Grains in Relation with the Gas and Stars: Diagnostic Tools

Thanks to their ubiquity, dust grains can be used to estimate several physical properties of their host galaxy.

2.4.1. Dust-related star-formation rate indicators. The SFR is a crucial quantity for galaxy evolution studies. Several dust-related SFR tracers have been empirically calibrated using observations of resolved star-forming regions in nearby galaxies. They rely on the fact that young stars are extremely luminous and are enshrouded with dust. If the clouds are optically thick and if their covering factor is unity, the OB star luminosity is $L_{OB} \simeq L_{TIR}$, where L_{TIR} is the total IR (TIR) luminosity. Contrary to a common misconception, this is independent of dust properties. Assuming a typical initial mass function (IMF), burst age, and metallicity, L_{OB} can be converted to SFR/($M_\odot$/year) $\simeq 10^{-10} \times L_{TIR}/L_\odot$. The contribution of old stars to L_{TIR} is negligible for sufficiently high SFRs. Alternatively, monochromatic SFR indicators have been proposed. Calzetti et al. (2007) and Li et al. (2010) found that the 24- and 70-µm monochromatic luminosities were good local SFR indicators (on spatial scales of $\simeq 0.5$–1 kpc): SFR/($M_\odot$/year) $\simeq 2,611 \times [L_\nu(24)/(L_\odot/Hz)]^{0.885}$ and SFR/($M_\odot$/year) $\simeq 1,547 \times L_\nu(70)/(L_\odot/Hz)$. In contrast, Peeters et al. (2004) found that, although the 6.2-µm UIB correlates with the SFR, it is probably a better tracer of B stars. Moreover, the UIB strength is strongly dependent on metallicity (see Section 4.3.4). Finally, several composite indicators have been calibrated (Hao et al. 2011, Boquien et al. 2016). By combining far-UV (FUV) or Hα measurements with 24-µm or TIR indicators, they account for the fact that star-forming regions are not completely opaque.

Dust-to-gas mass ratio: defined as $Z_{dust} = \Sigma_{dust}/\Sigma_{gas}$, where Σ_{gas} is the total gas mass surface density (HII, HI, and H$_2$, including He)

2.4.2. Estimating the total gas mass.

The complexity of ISM phase mixing makes the total gas mass difficult to estimate. Different, independent tracers are required for ionized versus neutral and for atomic versus molecular phases. Even when these tracers are available, some notable biases put the reliability of estimates into question: (*a*) The $[\text{HI}]_{21\,cm}$ emission can be saturated at high optical depths, leading to a possible underestimate of $N(\text{HI})$ by a factor of up to $\simeq 2$ (e.g., in the local ISM; see Fukui et al. 2015); (*b*) the $^{12}\text{CO}(J = 1 \rightarrow 0)_{2.6\,mm}$ emission, used to estimate $N(\text{H}_2)$, can be biased by the selective photodissociation of CO in translucent H$_2$ clouds, leading to a possible underestimate of $N(\text{H}_2)$ by a factor of up to $\simeq 100$ (e.g., in low-Z systems; see Madden et al. 1997). There is thus a reservoir of dark gas that is unaccounted for by these tracers. UV HI and H$_2$ absorption lines are less biased but are difficult to observe.

Whether observed in extinction or in emission, dust has been used as an indirect gas tracer for several decades (Hildebrand 1983, Devereux & Young 1990). Neglecting ionized gas and assuming that the HI surface density, Σ_{HI}, has been corrected for optical thickness, the dust surface density can be expressed as $\Sigma_{dust} = Z_{dust} \times (\Sigma_{\text{HI}} + \alpha_{\text{CO}} I_{\text{CO}})$, where Z_{dust} is the dust-to-gas mass ratio and α_{CO} is the conversion factor between the CO intensity, I_{CO}, and the H$_2$ surface density. Israel (1997) pioneered the derivation of α_{CO} in nearby galaxies using FIR dust emission. Leroy et al. (2011) designed a method to solve both for Z_{dust} and α_{CO}, assuming a homogeneous grain constitution and a constant Z_{dust} in each object studied. They confirmed that low-Z galaxies have larger α_{CO} than the MW (by a factor of up to $\simeq 20$). This well-established fact is believed to originate in the enhanced photodissociation of CO in an ISM that is less dusty and thus less opaque (see Section 4.3.2), while H$_2$ remains self-shielded. Similar studies have been done on extinction (e.g., in the LMC; see Dobashi et al. 2008).

2.4.3. Constraints for photodissociation models.

In PDRs, the gas is primarily heated by photoelectrons ejected from the grains (Draine 1978). The PE heating is most efficient for the smallest sizes, particularly for the carriers of the UIBs (see, e.g., Weingartner & Draine 2001). This heating efficiency therefore depends on the dust properties and thus on the environment. Assuming that $[\text{CII}]_{158\,\mu m}$ is the main gas coolant, the PE efficiency, ϵ_{PE}, can be approximated by the gas-to-dust cooling ratio: $\epsilon_{PE} \simeq L_{\text{CII}}/L_{\text{TIR}}$. Detailed studies usually add other lines to the gas cooling rate, such as $[\text{OI}]_{63\,\mu m}$, to have a more complete estimate (see, e.g., Cormier et al. 2015). Overall, Smith et al. (2017) found that $0.1\% \lesssim \epsilon_{PE} \lesssim 1\%$, with an average of $\langle \epsilon_{PE} \rangle \simeq 0.5\%$, in a sample of 54 nearby galaxies. It appears that ϵ_{PE} is lower when the dust temperature is higher (Rubin et al. 2009, Croxall et al. 2012). This is not likely the result of the destruction of the UIB carriers, as their intensity correlates best with the $[\text{CII}]_{158\,\mu m}$ emission (see, e.g., Helou et al. 2001). It is conjectured, rather, to result from the saturation of grain charging in UV-bright regions. The shape of the ISRF also has consequences for the accuracy with which L_{TIR} represents the true UV PE-efficient flux. Indeed, Kapala et al. (2017) showed that the variations of ϵ_{PE} in M31 could be explained by the contribution of old stars to L_{TIR}. Finally, one of the most puzzling features is that ϵ_{PE} is higher at low metallicity (Poglitsch et al. 1995, Madden et al. 1997, Cormier et al. 2015, Smith et al. 2017), while the UIB strength drops in these systems (see Section 4.3.4). This is currently poorly understood. However, in the extreme case of I Zw 18 ($Z \simeq 1/35\,Z_\odot$), where no UIB is detected and the PE heating is estimated to be negligible, the gas-cooling-to-TIR ratio is still $\simeq 1\%$ (Lebouteiller et al. 2017). In this instance, the gas could be heated by X-rays.

Studies focusing on gas properties usually run PDR models with built-in PE efficiency (see, e.g., Le Petit et al. 2006). In this case, dust parameters such as L_{TIR}, the visual attenuation, or the UIB strength help to refine the gas modeling (see, e.g., Chevance et al. 2016).
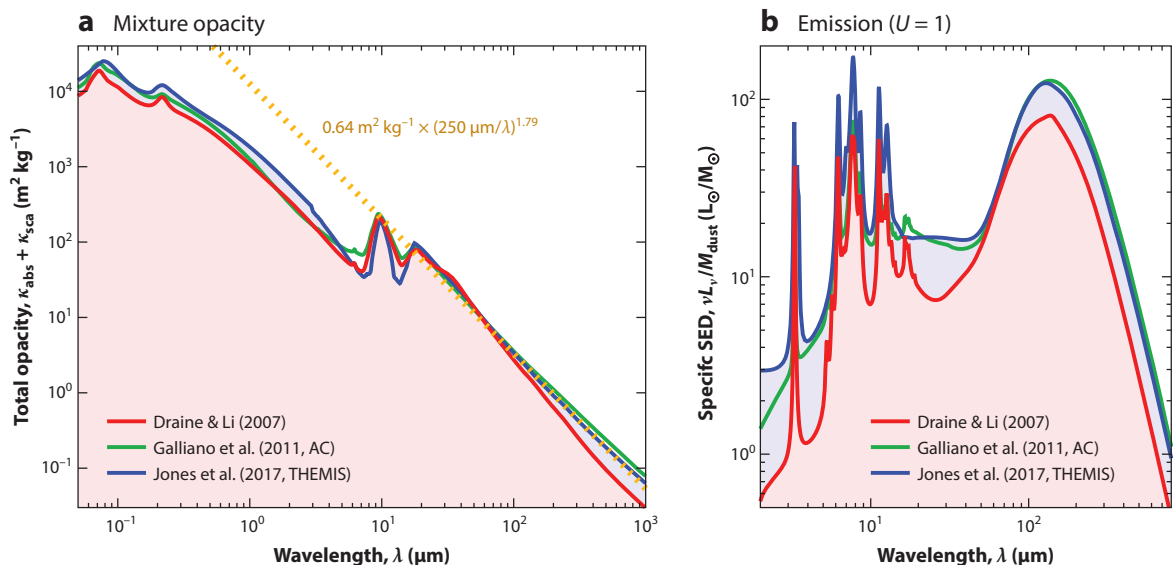
Figure 4

Emissivity of select dust models. (*a*) Extinction opacities. Notice the different submillimeter slopes. A power-law approximation to the model of Jones et al. (2017) is shown [*dashed yellow line*; $\beta = 1.79$, $\lambda_0 = 250$ μm, $\kappa(\lambda_0) = 0.64$ m^2/kg]. Here, κ_{abs} and κ_{sca} are the absorption and scattering opacities, respectively; β is the emissivity index and U is the starlight intensity. The green curve shows the AC model of Galliano et al. (2011), the red curve shows the model of Draine & Li (2007), and the blue curve shows THEMIS of Jones et al. (2017). (*b*) Corresponding emission. Abbreviations: AC, amorphous carbon; SED, spectral energy distribution; THEMIS, The Heterogeneous Dust Evolution Model for Interstellar Solids.

3. CONSTRAINTS ON THE MICROSCOPIC DUST PROPERTIES

3.1. Infrared Emission

Infrared emission is the most widely used observable to study grain properties.

3.1.1. Constraints on the far-infrared grain opacity. The dust mass and excitation derived from fits of the SED depend directly on the assumed grain opacity. To first order, this can be approximated by a power law in the FIR/submillimeter range (**Figure 4a**). Most studies assume a fixed absolute opacity, $\kappa(\lambda_0)$, and explore the variation of the emissivity index, β.

3.1.1.1. Studies of the emissivity index. There are numerous publications presenting MBB fits of nearby galaxies. However, as discussed in Section 2.3.1, the derived β_{eff} is degenerate with temperature mixing. The best constraints on the intrinsic β are obtained in the submillimeter regime, where only massive amounts of very cold dust ($T \lesssim 10$ K) could bias the value. **Table 1**

Table 1   Free emissivity index modified blackbody fits of nearby galaxies by the Planck Collaboration

	Milky Way	**M31**	**Large Magellanic Cloud**	**Small Magellanic Cloud**
T_{eff}	19.7 ± 1.4 K	18.2 ± 1.0 K	21.0 ± 1.9 K	22.3 ± 2.3 K
β_{eff}	1.62 ± 0.10	1.62 ± 0.11	1.48 ± 0.25	1.21 ± 0.27
Reference	Planck Collaboration (2014)	Planck Collaboration (2015b)	Planck Collaboration (2011a)	Planck Collaboration (2011a)

lists β_{eff} values for several objects, obtained with *Planck*, with constraints up to 850 μm. All the values are lower than 2, and low-Z systems appear to have a lower β_{eff} than high-Z galaxies. Boselli et al. (2012) studied a volume-limited sample with *Herschel* (up to 500 μm), finding an average $\beta_{eff} \simeq 1.5$, and suggested that low-Z objects tend to have $\beta_{eff} < 1.5$. In M33, β_{eff} derived from *Herschel* observations is about 2 in the center and decreases down to 1.3 in the outer parts (Tabatabaei et al. 2014). By contrast, the outer regions of M31 exhibit a steeper slope ($\beta_{eff} \simeq 2.3$) than that in the center (Draine et al. 2014). This contradictory behavior does not appear to originate in fit biases, as both increasing and decreasing trends of β_{eff} with radius are found in the sample of Hunt et al. (2015).

3.1.1.2. Constraints on the absolute opacity. The absolute opacity, $\kappa(\lambda_0)$, is totally degenerate with M_{dust} (Equation 1). The only way to constrain this quantity is to have an independent estimate of M_{dust}. For instance, Galliano et al. (2011) modeled the IR emission of a strip covering 1/4 of the LMC, using optical properties similar to those presented by Draine & Li (2007). The resulting dust-to-gas mass ratio was higher than the maximum number of elements that could be locked up in grains. This led Galliano et al. (2011) to propose a more emissive mixture (**Figure 4**) that could solve this inconsistency. The constraint on the elemental depletions was thus used to show that $\kappa(\lambda_0)$ should be a factor of $\simeq 2$–3 higher. Similarly, the Planck Collaboration (2016) modeled the all-sky dust emission using the model of Draine & Li (2007). However, the A_V estimated along the sightlines of $\gtrsim 200,000$ quasars was systematically lower than their dust emission–derived A_V. Their comparison of emission and extinction thus indicates that the Galactic opacity should also be a factor of $\simeq 2$ higher. Finally, in M31, Dalcanton et al. (2015) derived a high–spatial resolution map of A_V. As in the Galaxy, the emission-derived A_V map (Draine et al. 2014) was found to be a factor of $\simeq 2.5$ higher. We emphasize that, although each of these studies found evidence of local variations in the emissivity as a function of the density (see Section 4.2.1), the overall opacity seems to be scaled up compared to that presented by Draine & Li (2007). There is growing evidence that the dust opacities might be, in general, more emissive than standard uncoated compact silicate–graphite mixtures.

3.1.2. Aromatic feature spectrum. The MIR range exhibits a complex spectrum of ubiquitous emission bands that were originally labeled as UIBs (**Figure 5**). These bands are found in almost every environment. They were first detected in Galactic planetary nebulae (Gillett et al. 1973). Their relative intensity appeared to be independent of the position in reflection nebulae, leading to the conclusion that they were carried by very small, stochastically heated particles (Sellgren 1984).

3.1.2.1. Candidate materials. It is consensual, nowadays, that the UIBs arise from the vibrational spectrum of a collection of aromatic bonds in a hydrocarbon matrix (the weak 3.4-μm feature is attributed to aliphatic bonds; see Duley & Williams 1981). Polycyclic aromatic hydrocarbons (PAHs) were proposed by Léger & Puget (1984) and Allamandola et al. (1985). The UIBs likely arise from a statistical mixing of PAHs of different sizes and structures, averaging out drastic variations of the band profiles. Most studies interpret MIR spectra in light of this class of molecules. The main physical processes controlling the shape of the PAH spectrum are the following:

- Charge. PAH$^+$ ions have brighter 6–9-μm features than PAH^0 molecules, and the inverse holds for the other bands (**Figure 5b**). Select band ratios, such as $L_{7.7}/L_{11.3}$, increase with the charge.
- Size distribution. Small PAHs fluctuate up to temperatures higher than the large ones. Short-wavelength bands are therefore more pumped in small PAHs, whereas large PAHs emit predominantly long-wavelength features (**Figure 5b**).
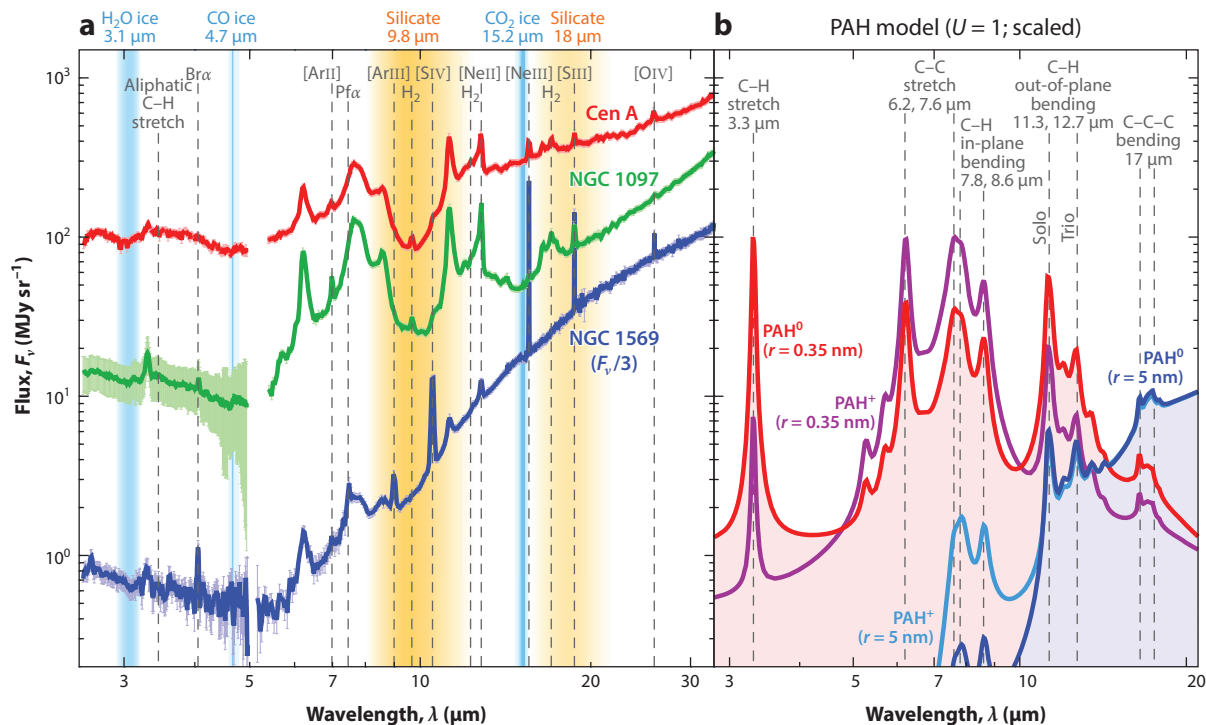
<div style="margin-left: left-margin">

Planck:
FIR–centimeter space telescope ($\lambda \simeq 300$ μm–1 cm; 2009–13)

PAH (polycyclic aromatic hydrocarbon): molecule composed of several aromatic cycles, with peripheral H atoms

</div>

Figure 5

Mid-infrared spectra. (*a*) *AKARI* (2.5–5 μm) and *Spitzer* (5–30 μm) spectra of the central regions of three galaxies (T. Roland & R. Wu, personal communication). Cen A is an early-type galaxy with an active galactic nucleus (AGN); it shows strong silicate absorption. NGC 1097 is a late-type starburst with a weak AGN. NGC 1569 is a blue compact dwarf, exhibiting weak unidentified infrared bands and strong ionic lines. (*b*) Theoretical emission of ionized and neutral polycyclic aromatic hydrocarbons (PAHs) (Draine & Li 2007), with radii *r*, heated by the diffuse Galactic interstellar radiation field ($U = 1$). These spectra are scaled by an arbitrary factor. The labels solo and trio represent one and three C–H bonds, respectively, on a given aromatic cycle.

- ISRF hardness. The hardness of the ISRF has an effect similar to the size, as a higher mean photon energy causes the grain to fluctuate up to higher temperatures (see, e.g., Galliano et al. 2008).

- Molecular structure. C–H out-of-plane bending modes have different frequencies, depending on the number of H atoms per aromatic cycle. The 11.3-μm band corresponds to a solo H, found on straight molecular edges, whereas the 12.7-μm one corresponds to a trio, found on corners of the molecules (**Figure 5b**). The solo/trio $L_{11.3}/L_{12.7}$ ratio is thus an indicator of PAH compactness (e.g., Hony et al. 2001).

- Foreground extinction. The wings of the silicate absorption feature at 9.8 μm selectively extinguish the 8.6- and 11.3-μm bands more than they extinguish the other features (for *AKARI* and *Spitzer* spectra, see **Figure 5a**).

- Dehydrogenation. This has a similar effect to ionization. However, for PAHs larger than $N_C \simeq 25$, hydrogenation through reactions with abundant atomic H is more important than H loss through unimolecular dissociation (see, e.g., Hony et al. 2001). Thus, dehydrogenation does not have a detectable effect on the UIB spectrum.

However, a mix of fully aromatic and/or partially hydrogenated molecules does not appear to give a completely satisfactory fit to the wavelength position and shape of the observed interstellar

AKARI:
space telescope
($\lambda \simeq 1.7$–180 μm;
2006–11)

emission bands in the 3.3–3.5-μm region (see, e.g., Sandford et al. 2013, figure 3). Alternatively, a-C(:H) nanoparticles, as in the model of Jones et al. (2017), could provide a physically viable alternative to the interstellar PAH hypothesis as carriers of the UIBs. To date, the interstellar dust model of Jones et al. (2017) appears to be the only one that is consistent with the presence of the emission bands at ≃3.3 and ≃3.4 μm and the associated sub-bands at ≃3.5 μm. In this model, these bands are due to a-C(:H) nanograins, of mixed aromatic, olefinic, and aliphatic composition, with size-dependent optical properties (Jones et al. 2013). Further, within the framework of Jones et al. (2017), variations in the band ratios in the 3.3–3.5-μm region can be explained by a-C(:H) compositional variations as the dust evolves in response to its environment. We adopt the generic term UIB because of the different alternative explanations for the phenomenon. Here, we refer to PAHs only when discussing results depending on the PAH hypothesis.

a-C(:H): amorphous carbon with partial hydrogenation, i.e., solids containing both aromatic and aliphatic bonds in a proportion depending on the H fraction

3.1.2.2. Mid-infrared spectrum fitting challenges. To study the properties of the UIBs, one needs to estimate the intensity of each band. Most studies perform least-squares spectral decompositions with the linear combination of several components (see, e.g., Smith et al. 2007, Galliano et al. 2008): (*a*) PAHs (Lorentz or Drude profiles), (*b*) gas lines (Gauss profiles), (*c*) a dust continuum (several MBBs), and (*d*) a stellar continuum. In addition, (*e*) the extinction by silicates and ices can be parameterized by their optical depths. However, as can be seen in **Figure 5a**, the wings of the UIBs can be difficult to distinguish from the dust continuum. In addition, several features are blended (e.g., the 6–9- and 17-μm complexes) and may present underlying broad plateaus. These bands can also be blended with ionic lines at low spectral resolution (e.g., the 12.7-μm band and the $[\text{NeII}]_{12.81\,\mu m}$ line). This type of fit can thus lead to some biases and degeneracies in the following cases (Galliano et al. 2008): (*a*) low signal-to-noise ratio, (*b*) low UIB-to-continuum ratio, and (*c*) moderate extinction. The derived band intensities are also sensitive to the adopted UIB positions and widths and on the nature and number of MBB components for the continuum.

3.1.2.3. Aromatic band ratios in nearby galaxies. Galliano et al. (2008) studied the 6.2-, 7.7-, 8.6-, and 11.3-μm UIBs in a sample of nearby galaxies and Galactic regions. Several band ratios were used in order to address the degeneracies between the effects of the charge, size distribution, ISRF hardness, and extinction. The $L_{6.2}/L_{11.3}$ and $L_{7.7}/L_{11.3}$ ratios vary by a factor of ≃10. Among this sample, covering a large range of physical conditions and spatial resolutions, it appears that most of the variations of the band ratios arise from variations of the PAH charge. Smith et al. (2007) also found large variations of the band ratios (by a factor of ≃2–5) in central regions of starbursts and AGNs. However, they found that the presence of a low-luminosity AGN could alter the spectrum by destroying the smallest PAHs (as confirmed by Sales et al. 2010). Harsh environments result in selective destruction of the smallest PAHs, as exemplified in elliptical galaxies (Kaneda et al. 2007, Vega et al. 2010) and in the superwind of M82 (Beirão et al. 2015).

In low-metallicity systems, the variations can be more difficult to probe, as the band equivalent widths are lower (**Figure 5a**; this point is discussed in Sections 4.2.3.1 and 4.3.4). In the LMC, Mori et al. (2012) found different trends in neutral and ionized sightlines. In the latter case, there is evidence that PAHs have a lower charge (as a consequence of the higher recombination rate) and are on average larger (due to the destruction of the smallest PAHs). In contrast, in the SMC, Sandstrom et al. (2012) found very weak $L_{6-9}/L_{11.3}$ ratios and weak 8.6- and 17-μm bands, implying small, weakly ionized PAHs. This last point is consistent with the trend of $L_{17}/L_{11.3}$ with Z found by Smith et al. (2007). However, Hunt et al. (2010) argued that blue compact dwarf (BCD) galaxies exhibit a deficit of small PAHs. If there is a smooth variation of PAH size distribution with Z, these results are in contradiction. Sandstrom et al. (2012) noted that these BCDs are more extreme environments than the SMC and that photodestruction could dominate PAH processing

(see Section 4.2.3.1). We note that the solution to this apparent controversy might alternatively reside in the difference in studied spatial scales. In the Magellanic clouds, *Spitzer* spectroscopy gives a spatial resolution of a few parsecs, compared to a few hundreds in nearby BCDs. The LMC and SMC exhibit strong spatial variations in their UIB spectra. Whelan et al. (2013) showed a diversity of MIR spectral properties in the SMC. They demonstrated that PAH emission in a region like N66 is dominated by its diffuse component, and not by its bright clumps, where PAHs are destroyed. At the other extreme, the molecular cloud SMC-B1#1 shows unusually high UIB equivalent widths (Reach et al. 2000). Also, the $L_{11.3}/L_{12.7}$ ratio indicates that PAHs are more compact in 30 Dor and more irregular outside it (Vermeij et al. 2002). All these elements suggest that there is a complex balance of processes shaping the MIR spectra throughout low-Z environments.

Finally, UIB ratios can be used as a diagnostic tool of the physical conditions. For instance, Galliano et al. (2008) provided an empirical calibration of the $L_{6.2}/L_{11.3}$ ratio with the UV-field-to-electron-density ratio, G_0/n_e (see Section 2.4.3). However, the dynamics of the UIB ratios being at most a factor of $\simeq 10$, with typical uncertainties of 20%, their diagnostic potential is practically limited to a low-/high-value dichotomy.

3.1.3. Silicate features in emission. Silicates are some of the most abundant dust species ($\simeq 2/3$ of the mass; Draine & Li 2007, Jones et al. 2017). They are characterized by two prominent features at 9.8 and 18 μm, corresponding to Si–O stretching and O–Si–O bending modes, respectively (**Figure 5a**). These features are most often seen in extinction (see Section 3.2.4). They can be seen in emission in galaxies when the dust is hot enough ($T \gtrsim 150$ K). This is the case near the central engine of AGNs (Wu et al. 2009, Hony et al. 2011), even in low-luminosity AGNs, such as the nucleus of M31 (Hemachandra et al. 2015). The MIR spectra of early-type galaxies also show clear silicate emission features, but likely of circumstellar origin (see, e.g., Bressan et al. 2006). Alternatively, some dust models present a significant out-of-equilibrium emission from small silicates (e.g., Zubko et al. 2004). Such small silicates are not unlikely (see, e.g., Section 3.5.6). In the diffuse ISM, the 9.8-μm feature would be hidden by the bright aromatic features. However, we should be able to see it when the UIB intensity decreases, as in dwarf galaxies. This is usually not the case (e.g., Rémy-Ruyer et al. 2015), perhaps suggesting either that these small silicates have not abundantly formed or that they are efficiently destroyed in dwarf galaxies.

3.1.4. Aliphatic feature in emission. The 3.4-μm aliphatic emission feature is carried by small a-C(:H). The $L_{3.4}/L_{3.3}$ aliphatic-to-aromatic ratio shows regional variations in the ISM as a result of structural changes in the hydrocarbons through UV processing (see, e.g., Jones et al. 2013). Yamagishi et al. (2012) detected this feature in the superwind of M82. They found that the $L_{3.4}/L_{3.3}$ ratio increases with the distance from the center. They interpreted this trend as the production of small a-C(:H) by shattering of larger grains in this harsh halo. Similarly, Kondo et al. (2012) found a higher $L_{3.4}/L_{3.3}$ ratio in the nuclear bar of NGC 1097, suggesting that the gas flow toward the center could lead to the formation of small a-C(:H) by shattering. We note that, alternatively, the $L_{3.4}/L_{3.3}$ ratio can increase with the accretion of a-C(:H) mantles in denser regions (Jones et al. 2013). This feature can also be seen in extinction in AGNs (see, e.g., Mason et al. 2007).

3.2. Wavelength-Dependent Extinction

Wavelength-dependent extinction is an important observable providing constraints on grain properties that are complementary to those provided by emission.
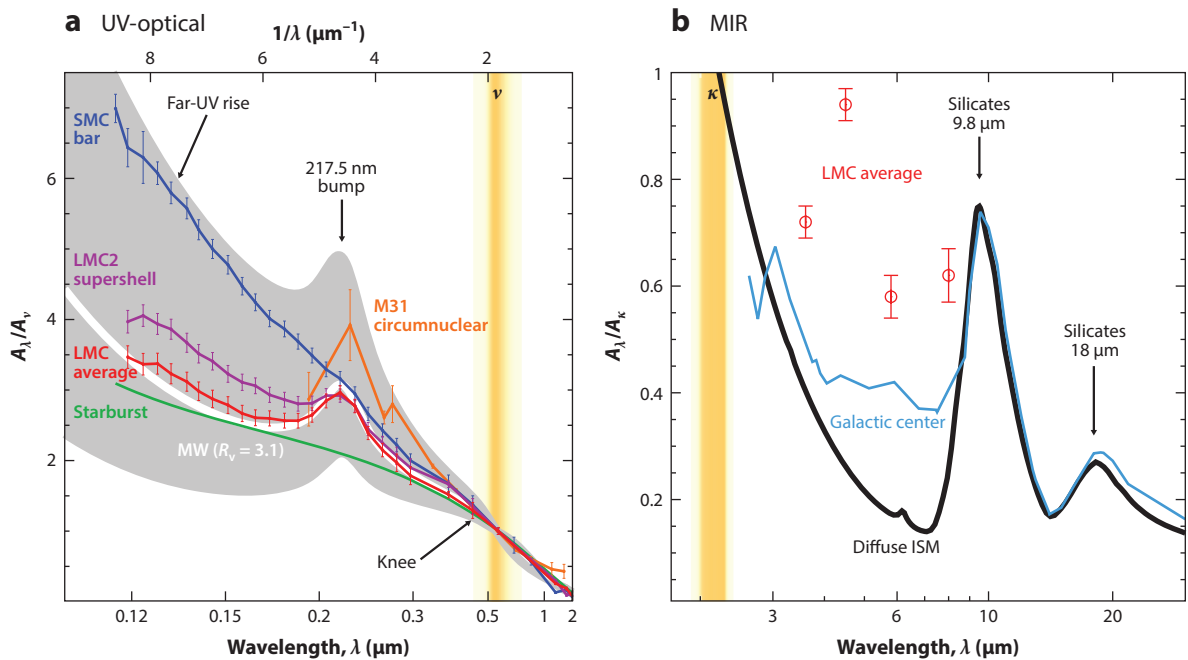
a UV-optical

$1/\lambda$ (μm^{-1})

SMC bar
Far-UV rise
217.5 nm bump
LMC2 supershell
M31 circumnuclear
LMC average
Starburst
MW ($R_V = 3.1$)
Knee
ν

A_λ/A_v

Wavelength, λ (μm)

b MIR

κ
LMC average
Silicates 9.8 μm
Silicates 18 μm
Galactic center
Diffuse ISM

A_λ/A_κ

Wavelength, λ (μm)

Figure 6

Extinction curves. (*a*) Extinction curves of the Magellanic clouds (Gordon et al. 2003) compared to the MW (the *gray area* spans $R_V = 2$–5, whereas the *white curve* corresponds to $R_V = 3.1$; Fitzpatrick 1999). Also displayed are the attenuation curve of starburst galaxies (Calzetti et al. 2000) and the attenuation curve of the circumnuclear region of M31 (Dong et al. 2014). (*b*) MIR LMC average (Gao et al. 2013) compared to the Galactic center (Lutz et al. 1996). Abbreviations: ISM, interstellar medium; LMC, Large Magellanic Cloud; MIR, mid-infrared; SMC, Small Magellanic Cloud; UV, ultraviolet.

3.2.1. General features. Extinction is a combination of light absorption and scattering. Early dust studies, before IRAS, were mainly based on extinction. In the MW, Cardelli et al. (1989) demonstrated that the UV-to-near-IR (NIR) extinction curves follow a universal law, parameterized by R_V:

$$R_V \equiv \frac{A_V}{A_B - A_V}, \quad \text{with} \quad A_\lambda = 1.086 \times \underbrace{[\overbrace{\kappa_{abs}(\lambda) + \kappa_{sca}(\lambda)}^{\text{intrinsic grain opacity}}] \times \overbrace{\Sigma_{dust}}^{\text{mass surface density}}}_{\text{optical depth, } \tau(\lambda)}. \qquad 3.$$

The sum of the absorption and scattering opacities, $\kappa_{abs} + \kappa_{sca}$, depends on the dust constitution. Such an extinction curve presents different regimes (**Figure 6a**): (*a*) a FUV rise, mainly caused by absorption by small grains (Rayleigh limit: $A_\lambda \propto 1/\lambda$); (*b*) a 217.5-nm absorption bump, probably carried by small carbon grains (PAHs, graphite, amorphous carbon, etc.); (*c*) an optical knee, mainly resulting from scattering by large grains; and (*d*) a power-law NIR continuum. On average, $R_V \simeq 3.1$ in the Galaxy, with large variations between sightlines ($R_V \simeq 2$–5) resulting from dust processing, with low values of R_V being attributed to regions with enhanced small grains. For a given R_V, the quantity $A_V/N(\text{H})$ is proportional to the dust-to-gas mass ratio.

3.2.2. Methodology. The most reliable wavelength-dependent extinction curves are derived using the pair method (Stecher 1965). Two stars of the same spectral type are observed, one with a low and one with a high foreground extinction. The extinction curve is directly derived from the

differential spectrum, assuming the dust properties are uniform along the two sightlines. In external galaxies, this method has been successfully applied only to the Magellanic clouds (see, e.g., Nandy et al. 1981, Gordon et al. 2003) and M31 (Bianchi et al. 1996, Clayton et al. 2015). Alternatively, a stellar atmosphere model can be used in lieu of the reference star (see, e.g., Fitzpatrick & Massa 2005).

In more distant objects, where observations of individual stars become impractical, other methods, less direct and more model dependent, have to be used. Stellar SED modeling with dust attenuation is widely used (see, e.g., Hutton et al. 2015). Attenuation, which is the net loss of photons within a galaxy, differs from extinction because it includes the effects of geometry. There is a degeneracy between dust attenuation and stellar age and metallicity. This degeneracy can be solved by accounting for FIR emission (Gordon et al. 2000) or by studying disks with different inclinations (Conroy et al. 2010). Alternatively, the ratio of H recombination lines can be used. Calzetti et al. (1994) derived an average attenuation law (**Figure 6a**) using this method, on a sample of 39 starbursts, assuming that all these objects had the same metallicity, stellar populations, and dust properties. This average curve is rather flat and has no bump (**Figure 6a**). In contrast, Conroy et al. (2010) derived an average attenuation law for disk galaxies based on UV–visible photometry. They found that the law of Calzetti et al. (1994) does not provide a good fit to their curve but that there might be a bump. They point out that it is possible that previous studies failed to recognize the presence of the UV bump because they tried MW laws only with $R_V = 3.1$.

Finally, other less common methods are available. In a few rare cases, a background lenticular galaxy can be used to probe the extinction in a foreground galaxy (see, e.g., White & Keel 1992, Berlind et al. 1997). Color magnitude diagrams can be used to probe visible–NIR extinction curves, such as the red giant clump (Gao et al. 2013, De Marchi & Panagia 2014). Supernovae (SNe) also provide bright sources for probing the extinction in the host galaxy (see, e.g., Patat et al. 2015).

3.2.3. Extragalactic results. External galaxies help us probe extinction curves in extreme conditions, beyond the simple R_V parameterization. There is continuous variation in the shape of the extinction curves from the Galaxy to the SMC (**Figure 6a**; Gordon et al. 2003). The SMC bar is characterized by a very steep curve ($R_V = 2.74 \pm 0.13$) without a 217.5-nm bump. This is a sign of a smaller grain size and a reduced fraction of carbon, likely the result of grain shattering by SN shock waves (Clayton et al. 2003, Cartledge et al. 2005). A weak bump is seen in the SMC wing, which is more quiescent. The LMC is intermediate between the Galaxy and the SMC, although there are important variations within. The LMC2 supershell, near the massive star-forming region 30 Dor, has a steeper law than the Galaxy ($R_V = 2.76 \pm 0.09$) with a weaker bump. The LMC average is closer to the Galaxy ($R_V = 3.41 \pm 0.28$). Neither the SMC nor the LMC2 supershell conforms to the parameterization of Cardelli et al. (1989). There still remain some uncertainties regarding these properties. De Marchi & Panagia (2014) studied the visible–NIR curve in 30 Dor, using the spread of the red giant clump in the color-magnitude diagram, and found a flatter extinction ($R_V \simeq 4.5$), which they attributed to freshly injected large grains.

The extinction curves of M31 ($Z = 1$–$1.5\ Z_\odot$) are consistent with those of the MW (Clayton et al. 2015, pair method). In its circumnuclear region, the curves appear steeper ($R_V \simeq 2.5$) but similar to the Galactic bulge (Dong et al. 2014, SED). In one of the regions studied by Dong et al. (2014), there is a significantly stronger UV bump (**Figure 6a**). In contrast, the spiral galaxy M101 appears to have a smaller bump, with a similar continuum (Rosa & Benvenuti 1994, SED). In the edge-on starburst M82, Hutton et al. (2015, SED) find that both R_V and the bump strength decrease outward with galactocentric distance. The spiral galaxies studied with the overlap method all exhibit MW curves (see, e.g., Dewangan et al. 1999, Deshmukh et al. 2013), as do early-type

galaxies (see, e.g., Goudfrooij et al. 1994, Finkelman et al. 2010). Some AGNs show signs of dust processing, having an absence of features (Crenshaw et al. 2001, Maiolino et al. 2001).

The extinction estimated toward SN II exhibits steep extinction curves ($R_V \simeq 1.5$), probably because of dust shattering by the shock wave (Hill et al. 1995, Amanullah et al. 2014, Hutton et al. 2015). The trend is the same toward SN I, with more dispersed values ($R_V \simeq 1.2$–3; Elias-Rosa et al. 2006, Huang et al. 2017).

3.2.4. Silicate features in absorption. In the MIR, the extinction curve is dominated by the two prominent silicate features at 9.8 and 18 μm (see Section 3.1.3; **Figure 6b**). In the Galaxy, $A_V/A_{9.8 \ \mu m} \simeq 12$. These absorption features can be seen when a sufficient amount of material is obscuring a bright MIR source (such as a star-forming region or an AGN). They are seen even at extremely low metallicity (for example, in SBS 0335-052, where $Z \simeq 1/35 \, Z_\odot$; Thuan et al. 1999, Houck et al. 2004). One issue is the composition of these silicates. It is well established that silicates are partially crystalline in circumstellar environments and become completely amorphous in the ISM (e.g., Kemper et al. 2004). The crystalline-to-amorphous ratio provides clues about dust processing, as crystallization and annealing have high energy barriers. For instance, Spoon et al. (2006) detected distinctive crystalline silicate absorption features in several ultraluminous infrared galaxies (ULIRGs). Their crystalline-to-amorphous fraction is $\simeq 10\%$. Spoon et al. interpreted this value as the result of a fresh injection of crystalline material by the massive star formation. On average, observations of nearby galaxies find mostly amorphous silicates. In a large sample of luminous infrared galaxies (LIRGs) and ULIRGs, Stierwalt et al. (2014) reported the detection of crystalline silicate absorption features in only 6% of their sample, in the most obscure sources.

3.2.5. Ice absorption features. In shielded regions, some molecules can freeze out to form icy grain mantles. The dominant species, H_2O, CO, and CO_2, produce MIR absorption bands (**Figure 5a**). In the Magellanic clouds, ice absorption can be studied in individual young stellar objects (see, e.g., Oliveira et al. 2013). In other galaxies, ice features likely come from molecular clouds. ULIRGs show particularly high ice optical depths that are correlated with the optical depth of silicates (Stierwalt et al. 2014). However, some galaxies with high silicate absorption do not present detectable ice features, suggesting that the density of the medium is not the only parameter; the presence of an AGN could prevent ice formation. In nearby star-forming galaxies, Yamagishi et al. (2015) conducted an extensive analysis of the CO_2-to-H_2O ice absorption ratio. This ratio exhibits variations of a factor of $\simeq 20$, as H_2O has a longer lifetime (higher sublimation temperature) than CO_2. They found that this ice ratio correlates best with specific SFR (sSFR), indicating a high ratio in young star-forming galaxies.

3.3. Elemental Depletion Patterns

Dust is made of the available heavy elements produced by stars. In the ISM, a fraction of these elements is in the gas, and the rest is locked up in dust. The fraction of missing elements from the gas is called depletion.

3.3.1. Definition and method. In the MW, where depletions have been studied for most relevant heavy elements, in several hundreds of sightlines through the diffuse neutral medium (Jenkins 2009), it appears that (*a*) refractory elements (elements with a higher condensation temperature, T_c) are more depleted than volatile elements (elements with a lower T_c) (see, e.g., Savage & Sembach 1996); and (*b*) the depletions increase the with mean density of the medium (see, e.g.,

Savage & Bohlin 1979, Crinklaw et al. 1994). The depletion of an element X is defined as

$$
\underbrace{\left[\frac{X_{gas}}{H}\right]}_{\text{depletion of X}} \equiv \underbrace{\log\left(\frac{X}{H}\right)_{gas}}_{\text{abundance of X}} - \underbrace{\log\left(\frac{X}{H}\right)_{ref}}_{\text{reference value}} \simeq \underbrace{\left[\frac{X_{gas}}{H}\right]_0}_{\text{minimum depletion}} + \underbrace{A_X \times F_\star}_{\text{local variation}}. \qquad 4.
$$

The second part of Equation 4 is a universal parameterization as a function of the depletion strength, $F_\star$ (Jenkins 2009). The minimum depletion term is thought to correspond to the core of the grain, whereas the varying environmental factor, $A_X F_\star$, is attributed to accretion of mantles in denser environments.

Depletion measurements provide a direct estimate of the dust content, independent of model assumptions. In addition, they provide constraints on the stoichiometry through the number ratio of available elements. These measurements are challenging, however. In the diffuse neutral medium (DNM), they are performed on absorption. Most of the transitions are in the UV and are thus inaccessible from the ground. Apart from possible line saturation and ionization corrections, the most challenging aspect is the adoption of reference abundances (Equation 4), representing the total ISM (gas and dust) abundances. Indeed, the different standards (solar, meteoritic, F and G stars, etc.) exhibit some inconsistencies. Alternatively, HII region abundances can be estimated from nebular lines. These estimates rely on photoionization modeling, which adds another layer of uncertainties.

3.3.2. Extragalactic depletions. In extragalactic systems, there have been numerous studies of DNM depletions in damped Lyα systems (DLAs; see, e.g., De Cia et al. 2016) and in γ-ray bursts (see, e.g., Friis et al. 2015), facilitated by the redshifting of the transitions in the visible range. Although such studies have usually been compelled to make corrections based on the MW, De Cia et al. (2016) adopted a holistic approach and derived self-consistent depletion sequences.

The depletions of several nearby galaxies have been studied. The most complete studies concern the Magellanic clouds, addressing several elements along several individual sightlines (see, e.g., Roth & Blades 1997, Welty et al. 1997, Sembach et al. 2001, Sofia et al. 2006, Tchernyshyov et al. 2015, Jenkins & Wallerstein 2017). Reference abundances can be estimated in situ directly from individual stars (see, e.g., Welty et al. 1997, Tchernyshyov et al. 2015). The main results are the following. (*a*) The LMC depletion pattern of most elements appears Galactic, the abundances being simply scaled down by the metallicity (Tchernyshyov et al. 2015). (*b*) In the SMC, there is a larger dynamics, likely resulting from more important processing (removal by shock waves). In addition, Si, Cr, and Fe are systematically less depleted, with the uncertainty in [Si/H]$_0$ being greater than its value, consistent with the value being 0 (Tchernyshyov et al. 2015). However, Jenkins & Wallerstein (2017)'s [Si/H]$_0$ is significantly larger than 0. Si depletion varies by a factor of $\simeq 2$ at nearly constant Fe depletions, suggesting a different condensation process (Tchernyshyov et al. 2015). (*c*) The C/O ratio is a factor of $\simeq 2$ below solar, in the Magellanic clouds, suggesting that the carbon-to-silicate grain mass fraction is lower (**Table 2**). (*d*) The Magellanic stream has a depletion pattern similar to that of the SMC (Sembach et al. 2001).

More extreme objects, such as the lowest-metallicity nearby galaxy I Zw 18 (Aloisi et al. 2003, Lebouteiller et al. 2013) and several star-forming galaxies (James et al. 2014), have been studied in absorption, with some uncertainties resulting from multiple sightlines with different physical conditions. Several studies based on HII emission lines focused on low-Z galaxies. It appears that [Mg/O] and [Mg/S] correlate with Z (Guseva et al. 2013), implying a higher Mg depletion at high Z. Similarly, [Fe/O] correlates with Z (see, e.g., Rodríguez-Ardila et al. 2005, Izotov et al. 2006). These results are qualitatively consistent with the trends for Magellanic clouds (**Table 2**).

Table 2 Abundances and depletions in the MW and the Magellanic clouds

X	C	O	Mg	Si	Fe	Mass ratio
MW						
$10^6(X/H)_{ref}$	290^{+30}_{-20}	580^{+70}_{-60}	42^{+2}_{-2}	41^{+2}_{-2}	35^{+2}_{-2}	$Z_\odot = 1/75$
$[X_{gas}/H]_0$ (%)	23^{+27}_{-23}	$2.3^{+12.3}_{-2.3}$	46^{+3}_{-4}	40^{+5}_{-5}	89^{+1}_{-1}	$Z_{dust}^{(F_\star=0)} = 1/330$
$[X_{gas}/H]_0 + A_X$ (%)	39^{+9}_{-11}	42^{+7}_{-8}	95^{+1}_{-1}	96^{+1}_{-1}	99^{+1}_{-1}	$Z_{dust}^{(F_\star=1)} = 1/140$
LMC						
$10^6(X/H)_{ref}$	87^{+25}_{-19}	320^{+90}_{-70}	18^{+4}_{-3}	22^{+6}_{-5}	21^{+4}_{-4}	$Z = 1/2\ Z_\odot$
$[X_{gas}/H]_0$ (%)	$\simeq 31^a$	$\lesssim 20^a$	NA	52^{+3}_{-3}	89^{+1}_{-1}	$Z_{dust}^{(F_\star=0)} = 1/750$
$[X_{gas}/H]_0 + A_X$ (%)	NA	NA	NA	94^{+1}_{-1}	99^{+1}_{-1}	$Z_{dust}^{(F_\star=1)} = 1/250$
SMC						
$10^6(X/H)_{ref}$	33^{+9}_{-7}	140^{+30}_{-20}	$7.6^{+1.2}_{-1.1}$	$9.1^{+2.7}_{-2.0}$	$7.8^{+1.6}_{-1.4}$	$Z = 1/5\ Z_\odot$
$[X_{gas}/H]_0$ (%)	$\simeq 28^a$	$\simeq 32^a$	49^{+6}_{-6}	40^{+3}_{-3}	89^{+1}_{-1}	$Z_{dust}^{(F_\star=0)} = 1/2,760$
$[X_{gas}/H]_0 + A_X$ (%)	NA	NA	71^{+11}_{-18}	95^{+1}_{-1}	99^{+1}_{-1}	$Z_{dust}^{(F_\star=1)} = 1/630$

MW: Solar abundance compilation and depletions are from Jenkins (2009). LMC: Stellar abundance compilation and depletions are from Tchernyshyov et al. (2015); [C/H] and [O/H] are from Korn et al. (2002). SMC: Stellar abundance compilation is from Tchernyshyov et al. (2015); depletions are from Jenkins & Wallerstein (2017); [C/H] is from the HII modeling of NGC 456 done by Peña-Guerrero et al. (2012); [O/H] is derived from the [O/Zn] [Sk 108, $\log N(HI) = 20.5 \Rightarrow F_\star \simeq 0$] of Mallouris (2003) and the [Zn/H] of Jenkins & Wallerstein (2017). Abbreviations: LMC, Large Magellanic Cloud; MW, Milky Way; NA, not available; SMC, Small Magellanic Cloud.
[a] Estimate from nebular emission lines.

3.4. Polarization Studies

Grains are some of the main agents polarizing light in galaxies. Historically, Hall (1949) and Hiltner (1949) first noted that starlight was sometimes polarized by a small percentage and that the degree of polarization was correlated with the reddening. Davis & Greenstein (1951) proposed that this polarization was caused by nonspherical grains. Stein (1966) predicted that the emission by such elongated grains should also produce polarized IR emission. Dolginov & Mitrofanov (1976) proposed radiative torques as the main mechanism of grain alignment. Recently, the whole-sky polarization map of the Galaxy, at 353 GHz (1° resolution), was observed by *Planck*. The submillimeter polarization fraction can be as high as 20% in the most diffuse regions [$N(H) \simeq 10^{20}$ H/cm^2] and decreases along the densest sightlines [$N(H) \simeq 10^{22}$ H/cm^2; Planck Collaboration 2015a]. In the low-density regime, this behavior is consistent with turbulently disordered magnetic field orientations. In regions of higher densities, which are more opaque, the trend can be explained by a decrease in the efficiency of radiative torque alignment.

In nearby galaxies, polarization studies have been conducted at all wavelengths from FUV to radio. Dust-induced polarization (see the sidebar titled Dust-Induced Polarization Processes) is usually used to trace one of three phenomena described in Sections 3.4.1, 3.4.2, and 3.4.3.

3.4.1. Geometry of complex regions. Polarization can provide information on the geometry of unresolved or poorly constrained sources. Notably, the polarimetric observations of the central region of the archetypal Seyfert 2 galaxy NGC 1068 were interpreted as the scattering of light from the central accretion disk, obscured by a dusty torus (Antonucci & Miller 1985). These results were a major step toward the unified AGN model, attributing the differences in observed properties of Seyfert galaxies to the difference in orientation of the central source (Antonucci

DUST-INDUCED POLARIZATION PROCESSES

- In **scattering**, the light from a bright source (a star or AGN) scattered onto grains is partially polarized. The resulting fraction of linear polarization is a complex function of the dust composition, size, and spatial distribution. This process is usually efficient in the UV (see, e.g., Zubko & Laor 2000). It applies equally to spherical and elongated grains. Most radiative transfer models include this polarization mechanism.
- In **dichroic extinction**, the light from a background source seen through a cloud of magnetically aligned elongated grains is partially polarized perpendicular to the magnetic field. In the MW, the wavelength-dependent linear polarization fraction caused by this process follows the law of Serkowski et al. (1975). It is efficient from the near-UV to the NIR, peaking at about $\lambda \simeq 0.55\ \mu m$.
- In **dichroic emission**, the thermal emission from magnetically aligned elongated grains is polarized parallel to the magnetic field. The wavelength-dependent fraction of linear polarization is rather flat over the whole FIR-to-submillimeter regime (see, e.g., Guillet et al. 2018).

1993). Apart from AGN, NIR polarimetry of M82 has contributed by revealing a central nuclear star-forming ring (Dietz et al. 1989).

Polarization studies have also shed light on the nature of diffuse UV halos of star-forming galaxies: Are they made purely of scattered light, or is there a faint stellar population? Observations of edge-on galaxies, such as NGC 3125 (Alton et al. 1994) and M82 (Yoshida et al. 2011), have revealed that their dusty outflows were scattering light from the central starburst. Cole et al. (1999) also studied the polarization of star-forming regions in the LMC to constrain the extent of their UV halos.

3.4.2. Structure of the magnetic field. In case of dichroic extinction or emission, the polarization angle provides a map of the projected magnetic field. Studies were performed in the NIR–visible range on, among others, NGC 891 (Montgomery & Clemens 2014), M82 (Greaves et al. 2000, Jones 2000), the SMC (Lobo Gomes et al. 2015), NGC 6946 (Fendt et al. 1998), and the dust lane of Cen A (Scarrott et al. 1996).

3.4.3. Dust composition. The wavelength-dependent shape of the polarization fraction provides valuable information on the dust constitution. In particular, studies of M31 (Clayton et al. 2004), M82 (Kawabata et al. 2014), the LMC (Clayton et al. 1996), and the SMC (Rodrigues et al. 1997) all concluded that the polarizing grains were smaller in these objects than in the MW. Polarimetry can also be used to discriminate between models. For instance, Mason et al. (2007) studied the polarization of the 3.4-μm aliphatic band in order to test the silicate core/organic mantle model (Li & Greenberg 2002). They observed the interstellar medium of NGC 1068 in absorption toward its central engine. If the carriers of the 3.4-μm band were associated with large grains, the feature would be significantly polarized, which is not the case.

3.5. Dust-Related Epiphenomena

Emission, extinction, depletion, and polarization are the main observables that dust models attempt to reproduce. Several other processes, although less studied and poorly understood, could nonetheless reveal important information about grain properties in the future.

3.5.1. Dust observables in X-rays.
Dust absorbs and scatters X-rays. This fact has been used by researchers in several ways. First, the photoelectric absorption edges of elements locked up in grains contain potential information on their chemical structure (see, e.g., Lee et al. 2009). For instance, Zeegers et al. (2017) studied the Si K-edge along the line of sight of a Galactic X-ray binary. They were able to constrain the column density and the chemical composition of the silicate grains. Second, X-ray scattering halos can be used to constrain dust models (see, e.g., Smith et al. 2016). As an illustration, Corrales & Paerels (2015) modeled the X-ray halo around Cygnus X-3. They were able to put constraints on the size distribution, especially on the large grain cutoff. Last, Draine & Bond (2004) made a case that time-varying X-ray halos could be used to estimate distances of nearby galaxies, down to 1% accuracy for M31.

Among external galaxies, the dust-scattering X-ray halos of several γ-ray bursts have been observed (see, e.g., Evans et al. 2014). To our knowledge, however, no such study has been conducted in nearby galaxies.

3.5.2. Diffuse interstellar bands.
Diffuse interstellar bands (DIBs) are ubiquitous absorption features in the $\simeq 0.4$–2-μm range. Over 400 of them have been detected in the ISM (Hobbs et al. 2009) since their discovery a century ago (Heger 1922). They remain largely unidentified, although four of them have been attributed to C_{60}^{+} (Campbell et al. 2015). They are associated to dust, as their strength correlates with $E(B-V)$ at low values, but they disappear in denser sightlines (see, e.g., Lan et al. 2015). To first order, DIBs correlate with each other, but there are some notable differences, suggesting that they have different carriers (Herbig 1995). For instance, the so-called C_2 DIBs (Thorburn et al. 2003) appear to be found preferentially in diffuse molecular clouds.

DIBs are abundantly observed in external galaxies, including distant objects such as DLAs (see, e.g., Lawton et al. 2008). As a narrow spectral feature, they can easily be separated in velocity from the foreground Galactic features. They are observed in the ISM of nearby galaxies along the lines of sight of (*a*) stars [for example, in M33 (Cordiner et al. 2008), M31 (Cordiner et al. 2011), and the Magellanic clouds (Welty et al. 2006, van Loon et al. 2013, Bailey et al. 2015)]; (*b*) SN II [for example, in Cen A (Phillips et al. 1987, D'Odorico et al. 1989), M66 (Bolte et al. 1989), the LMC (Vidal-Madjar et al. 1987), M100 (Cox & Patat 2008), M82 (Welty et al. 2014)]; (*c*) SN Ia (see, e.g., Sollerman et al. 2005, Huang et al. 2017); and (*d*) lenticular galaxies (Ritchey & Wallerstein 2015).

In galaxies that are normal and have solar metallicity, the strengths of the DIBs and their relation to A_V seem to be similar to those of the MW (Heckman & Lehnert 2000, Sollerman et al. 2005, Cordiner et al. 2011, Huang et al. 2017), although some differences can be found (e.g., for M100, see Cox & Patat 2008; for M33, see Cordiner et al. 2008; and for M82, see Welty et al. 2014). In contrast, the largest deviations are found in the Magellanic clouds. Welty et al. (2006) reported that the DIBs are weaker in the LMC and SMC compared to in the MW by factors of $\simeq 7$–9 and $\simeq 20$, respectively. However, they found that the C_2 DIBs have the same strength per H atom as in the Galaxy. DIB spectra appear to be controlled by the UV field intensity (Cox et al. 2006), with disappearance of the features in the ionized gas or in a high-UV field (van Loon et al. 2013, Bailey et al. 2015). DIB strength also scales with metallicity, due to both lower shielding and lower elemental abundances (Cox et al. 2007, Bailey et al. 2015). Finally, DIBs appear to be linked with the shape of the extinction curve. Cox et al. (2007) demonstrated that, in the SMC, the sightlines with a weak or nonexistent 2,175-Å bump are those with weak or nonexistent DIBs.

3.5.3. Grain photoluminescence.
Photoluminescence is a nonthermal emission process in which, subsequently to the absorption of a UV photon, a grain is brought to an excited electronic state. After partial internal relaxation, a redder photon is emitted, bringing the electron back to

its fundamental state. Extended red emission (ERE), which is a broad emission band found in the ≃0.6–0.9-μm range of a variety of Galactic environments, is attributed to dust photoluminescence (see, e.g., Witt & Vijh 2004). The nature of its carriers is still debated.

In nearby galaxies, ERE has been spectroscopically detected in the star-forming region 30 Dor (LMC; Darbon et al. 1998), in M82 (Perrin et al. 1995), and in NGC 4826 (Pierini et al. 2002). In the dwarf galaxies SBS 0335-052 and NGC 4449, Reines et al. (2008a,b) modeled the photometric observations of several super star clusters (SSCs). Their results exhibit a significant I-band excess that they attributed to ERE. However, Reines et al. (2010) admitted that this excess could be accounted for by continuum and line emission of the ionized gas in NGC 4449.

3.5.4. Near-infrared excess.
An excess emission above the extrapolated stellar continuum is often detected in the NIR range (Joseph et al. 1984, Hunt & Giovanardi 1992). It is seen in disk galaxies (see, e.g., Lu et al. 2003, Boquien et al. 2011) and dwarf galaxies (see, e.g., Vanzi et al. 2000, Smith & Hancock 2009). It potentially hampers our ability to accurately estimate stellar mass from NIR photometry. This excess could be due to (a) nebular emission (the Brα line and the free–free continuum; see, e.g., Smith & Hancock 2009); (b) hot equilibrium dust (see, e.g., Vanzi et al. 2000), probably in circumstellar disks (Wood et al. 2008); or (c) out-of-equilibrium small grains (see, e.g., Boquien et al. 2010).

Studying disk galaxies, Lu et al. (2003) describe this excess, having a color temperature of ≃10^3 K and an intensity of a few percent of the total FIR. They found this excess to correlate with the UIB intensity. In general, this excess correlates with SFR indicators (Boquien et al. 2010, Mentuch et al. 2010). The emissivity of the three proposed phenomena listed above correlates with star-formation activity. In a filament of the BCD NGC 1569 Onaka et al. (2010) showed spectroscopically that the nebular emission cannot account for the excess, thus favoring hot dust.

3.5.5. Submillimeter excess.
An excess emission above the modeled dust continuum is often detected, longward ≃500 μm. The most significant reports of this submillimeter excess cannot be accounted for by free–free, synchrotron, and molecular line emission (**Figure 1**; see also Galliano et al. 2003). The first occurence of such an excess was unveiled by Reach et al. (1995), studying the COBE observations of the MW. Their IR-submillimeter SED could be fitted with a MBB ($\beta = 2$; see Section 2.3.1.1) and an additional 4–7 K component. A few years later, Lisenfeld et al. (2002) and Galliano et al. (2003) found a statistically significant excess in the dwarf galaxy NGC 1569, at 850 μm and 1.3 mm. Several subsequent studies confirmed the presence of an excess in other late-type galaxies (see, e.g., Dumke et al. 2004, Bendo et al. 2006, Galametz et al. 2009), including the global SEDs of the Magellanic clouds (Israel et al. 2010, Bot et al. 2010). *Herschel* and *Planck* opened the way to more detailed tests. In particular, Paradis et al. (2012) showed that the 500-μm excess becomes significant in the peripheral regions of the MW (>35°), as well as toward some Hɪɪ regions. Its relative amplitude can be up to ≃20%. Spatially resolved observations of the LMC have shown that the 500-μm excess varies up to ≃40% in certain regions and is anticorrelated with the dust surface density (Galliano et al. 2011). When resolved in nonbarred spirals, the submillimeter excess is primarily detected in the disk outskirts, and thus at low surface density (see, e.g., Hunt et al. 2015).

3.5.5.1. Reality of the phenomenon.
First, we emphasize that, by definition, this excess is model dependent. Different dust opacities lead to different amplitudes of the excess. For this reason, probing this excess with models that are not based on realistic optical properties is not appropriate. Second, the shape of the SED is well characterized in this regime. It has been observed at different wavelengths and with different instruments. It is still present with the latest *Herschel*

calibration (Dale et al. 2017). In addition, reports of a deficit are very rare. Finally, the Planck Collaboration (2011a) showed that, whereas the submillimeter excess in the integrated SED of the LMC was consistent with cosmic microwave background (CMB) fluctuations, the SMC excess was significantly above this level.

WMAP: *Wilkinson Microwave Anisotropy Probe* ($\lambda \simeq 3.2$–13 mm; 2001–10)

3.5.5.2. Possible explanations. The origin of the excess is currently being debated. The following explanations have been proposed.

- Very cold dust (VCD) can be used to fit the excess. However, it leads to massive amounts of grains. Galliano et al. (2003) showed that VCD would be realistic only if this component were distributed in a few number of dense, parsec-size clumps. Using spatially resolved observations of the 500-μm excess in the LMC, Galliano et al. (2011) concluded that this explanation is unrealistic.
- Temperature-dependent emissivity: The model of Meny et al. (2007) predicts an increase of $\kappa(\lambda_0)$ and a decrease of β with the temperature of amorphous grains. It reproduces the MW excess (Paradis et al. 2012) and the LMC excess (Bot et al. 2010, coupled with spinning grains; see also Section 3.5.6). However, it cannot account for the excess in the SMC (Bot et al. 2010).
- Magnetic grains: Draine & Hensley (2012) showed that the SMC excess could be attributed to magnetic nanoparticles (Fe, Fe_3O_4, and γ-Fe_2O_3). Thermal fluctuations in the magnetization of these grains can produce strong magnetic dipole emission, since ferromagnetic materials are known to have large opacities at microwave frequencies. This hypothesis seems to be consistent with the observed elemental abundances of the SMC and could also be responsible for the excess detected in other environments.

3.5.6. Spinning grains. Anomalous microwave emission (AME) is a centimeter-continuum excess that cannot be accounted for by the extrapolation of dust models or by free–free, synchrotron, and molecular line emission (**Figure 1**). It was first detected in the MW (Kogut et al. 1996). Draine & Lazarian (1998) promptly proposed that it arises from the dipole emission of quickly rotating ultrasmall grains. The candidate carriers were thought to be PAHs. WMAP (*Wilkinson Microwave Anisotropy Probe*) and *Planck* data of the Galaxy were successfully fitted with spinning dust models, including PAHs (see, e.g., Planck Collaboration 2011b). In the MW, AME correlates with all tracers of dust emission (Hensley et al. 2016). However, Hensley et al. (2016) showed that the AME-to-TIR ratio does not correlate with the PAH abundance. These authors thus proposed that the carriers of the AME could be nanosilicates rather than PAHs.

In nearby galaxies, the first unambiguous detection of AME has been obtained in an outer region of NGC 6946 (Murphy et al. 2010, Scaife et al. 2010). Subsequent observations showed evidence for AME in eight regions of this galaxy (Hensley et al. 2015). This study showed that the spectral shape of this AME is consistent with spinning dust, but with a stronger AME-to-PAH-surface-density ratio, hinting that other grains could be the carriers. Overall, the AME fraction is highly variable in nearby galaxies. Peel et al. (2011) put upper limits on the AME in M82, NGC 253, and NGC 4945. These upper limits suggest that, in these objects, AME/100 μm is lower than in the MW. In M31, the Planck Collaboration (2015b) reported a 2.3σ measurement of AME, consistent with Galactic properties. Finally, Bot et al. (2010), fitting the NIR-to-radio SED of the LMC and SMC, tentatively explained the submillimeter/millimeter excess with the help of spinning dust, in combination with a modified submillimeter dust emissivity (see Section 3.5.5). They conclude that if spinning grains are responsible for this excess, their emission must peak at 139 GHz (LMC) and 160 GHz (SMC), implying large ISRF intensities and densities. Draine

DUST EVOLUTION PROCESSES

- In **grain formation**, the dust mass is built up by (*a*) grain condensation in the ejecta of core-collapse SNe and AGB stars and (*b*) grain (re-)formation in the ISM by accretion of atoms and molecules (grain growth and mantle and ice formation).
- In **grain processing**, the grain constitution is altered in the ISM by (*a*) shattering and fragmentation by grain–grain collisions in low-velocity shocks (modification of the size distribution), (*b*) structural modifications by high-energy photon or cosmic ray impacts, and (*c*) coagulation.
- In **grain destruction**, the elements constituting the grains are partially or fully removed by (*a*) erosion and evaporation by thermal or kinetic sputtering (gas–grain collision in a hot gas or a shock), (*b*) photodesorption of atoms and molecules, (*c*) thermal evaporation, and (*d*) astration (incorporation into stars).

& Hensley (2012) argued that such quickly rotating grains would need a PDR phase with a total luminosity more than two orders of magnitude brighter than the SMC.

4. EVIDENCE OF DUST EVOLUTION

4.1. The Empirical Effects of Star-Formation Activity and Metallicity

Dust evolution is the modification of the constitution of a grain mixture under the effect of environmental processing. Most dust evolution processes (for a list, see the sidebar titled Dust Evolution Processes) can be linked to star formation: (*a*) formation and subsequent evaporation of molecular clouds; (*b*) stellar ejecta; (*c*) SN shock waves; and (*d*) UV and high-energy radiation. The characteristic timescale of these processes is relatively short (of the order of the lifetime of massive stars; $\tau \lesssim 10$ Myr), and their effect is usually localized around the star-forming region. For these reasons, the sSFR is an indicator of sustained dust processing. However, the dust lifecycle is a hysteresis. There is a longer-term evolution, resulting from the progressive elemental enrichment of the ISM, which becomes evident on timescales of $\simeq 1$ Gyr. This evolutionary process can be traced by the metallicity.

These two evolutionary timescales have an impact on the integrated SEDs of nearby galaxies. **Figure 7** illustrates that the effects of star-formation activity and metallicity are not always easy to disentangle. Indeed, low-*Z* systems are often dominated by young stellar populations. In addition, their lower dust-to-gas mass ratio renders their ISM more transparent and thus allows massive star formation to impact the ISM in a larger volume (see Section 2.1.3). In other words, some properties of dwarf galaxies may be the result of their hard and intense radiation field rather than their low metallicity. In practice, dust evolution processes can be probed by comparing regions in a galaxy or by comparing integrated galaxies. Our ability to observe ISM dust evolution in real time is limited to SN remnants (e.g., SN 1987A; Dwek et al. 2010).

4.2. Localized Dust Processing

Short-timescale dust evolution processes affect the ISM locally around the source of the process (e.g., star cluster, SN remnant, molecular cloud). They can thus be evidenced in spatially resolved observations of galaxies.
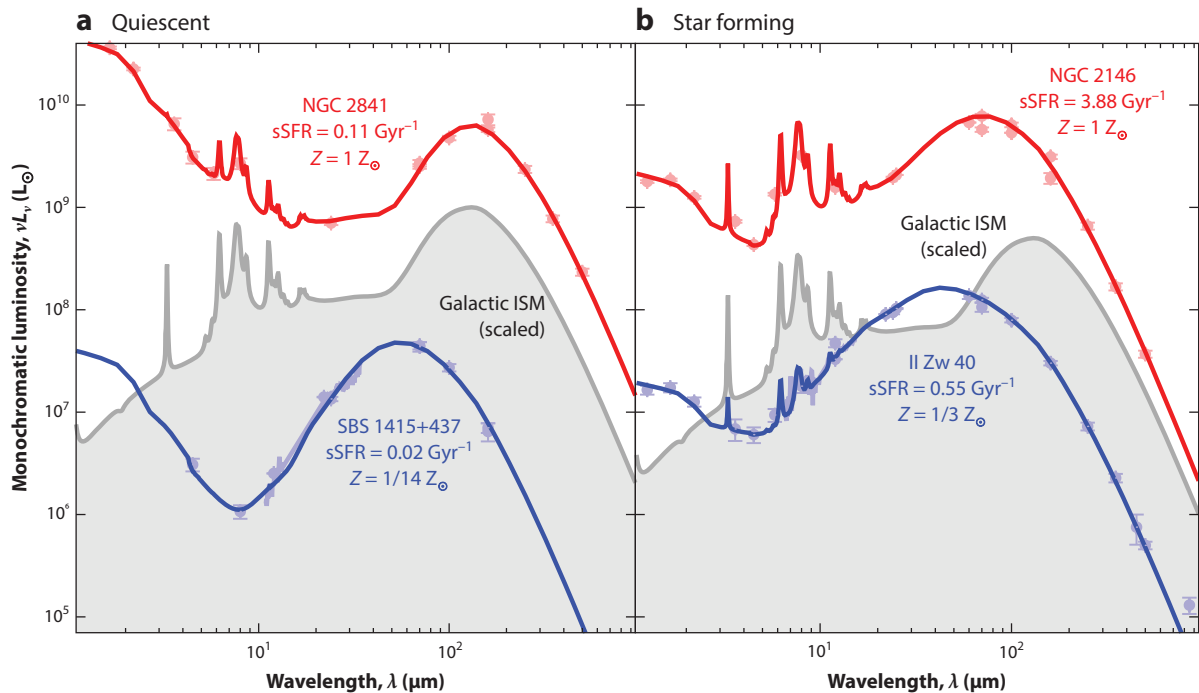
a Quiescent

b Star forming

NGC 2841
sSFR = 0.11 Gyr⁻¹
Z = 1 Z⊙

Galactic ISM
(scaled)

SBS 1415+437
sSFR = 0.02 Gyr⁻¹
Z = 1/14 Z⊙

NGC 2146
sSFR = 3.88 Gyr⁻¹
Z = 1 Z⊙

Galactic ISM
(scaled)

II Zw 40
sSFR = 0.55 Gyr⁻¹
Z = 1/3 Z⊙

Monochromatic luminosity, νL_ν (L⊙)

Wavelength, λ (μm)

Figure 7

Effects of dust evolution on the spectral energy distributions (SEDs) of galaxies. Each panel displays the observations and the SED model of two nearby galaxies (Rémy-Ruyer et al. 2015), in addition to the SED of the diffuse Galactic interstellar medium (ISM) (*gray*). (*a*) The red curve shows a quiescent solar metallicity galaxy. Apart from the stellar continuum, it is identical to the diffuse ISM. In contrast, the blue curve represents a low-metallicity quiescent system. Its dust properties are notably different, having weak or absent UIBs; overall hotter dust (FIR peaks at shorter wavelengths); and a broader FIR spectrum, resulting from a distribution of starlight intensities and/or an overabundance of small grains (see Section 2.3.1.2). This SED is qualitatively similar to the SED of a compact H II region (see, e.g., Peeters et al. 2002). (*b*) The red curve shows a solar metallicity galaxy with sustained star-formation activity. Compared to its quiescent counterpart, it has a much hotter and broader FIR emission, originating at least partly in bright photodissociation regions. The blue curve, showing a starbursting low-*Z* galaxy, has the same features as its quiescent counterpart, with a broader FIR emission. Other abbreviation: sSFR, specific star-formation rate.

4.2.1. Grain growth. There is clear evidence of FIR opacity variation in the MW. The main factor seems to be the density of the medium. For instance, Stepnik et al. (2003) found that the FIR dust cross section per H atom increases by a factor of $\simeq 3$ from the diffuse ISM to the molecular cloud they targeted. They noticed that this opacity variation is accompanied by the disappearance of the small grain emission. They concluded that grain coagulation could explain these variations (see also Köhler et al. 2015). In the diffuse ISM, Ysard et al. (2015) showed that the variation of emissivity, including the β–T relation (see Section 2.3.1.1), could be explained by slight variations of the mantle thickness in the model of Jones et al. (2017). This observed behavior is also consistent with the progressive demantling and disaggregation of molecular cloud-formed, mantled, and coagulated grains injected into the low-density ISM following cloud disruption. It is perhaps not unreasonable to hypothesize that dust growth in the ISM occurs on short timescales during cloud collapse rather than by dust growth in the quiescent diffuse ISM. In this alternative interpretation, the arrow of time is in the opposite sense and requires rapid dust growth, through accretion and coagulation, in dense molecular regions and slow demantling and disaggregation in the diffuse ISM.

In nearby galaxies, such studies are difficult to conduct, as the emissivity variations are smoothed out by the mixing of dense and diffuse regions. Even when potential evolutionary trends are observed, their interpretation is often degenerate with other factors. The Magellanic clouds are the most obvious systems where this type of study can be attempted. The insights provided by depletion studies (see Section 3.3) show that there are clear variations in the fraction of heavy elements locked up in dust, and these variations correlate with the density (Tchernyshyov et al. 2015, Jenkins & Wallerstein 2017). Since the coagulation and the accretion of mantles lead to an increase in FIR emissivity (e.g., Köhler et al. 2015), we should expect emissivity variations in the Magellanic clouds. Indeed, Roman-Duval et al. (2017) studied the trends of gas surface density (derived from HI and CO) as a function of dust surface density (derived from the IR emission) in these galaxies. They found that the observed dust-to-gas mass ratio of the LMC increases smoothly by a factor of $\simeq 3$ from the diffuse to the dense regions. In the SMC, the same variation occurs, with a factor of $\simeq 7$. They argue that optically thick HI and CO-free H_2 gas (see Section 2.4.2) cannot explain these trends and that grain growth is thus the most likely explanation. However, we note that the possible increase of the dust opacity with density could explain part of this trend.

4.2.2. Size distribution variations.
As we have seen in Section 3.2, there is a great diversity of extinction curves in the MW and in nearby galaxies. A large part of these variations is thought to be the result of variations in the size distribution, with a small R_V corresponding to an overabundance of small grains (see, e.g., Cartledge et al. 2005). Comparing the SMC bar to the SMC wing or the LMC2 supershell to the LMC average (**Figure 6**), it appears that there are more small grains in regions of massive star formation. In the same way, comparing the extinction curves in the MW, LMC, and SMC, we also notice that there is a potential increase of the small-grain fraction when the metallicity decreases. As pointed out in Section 4.1, the two effects are degenerate.

Constraining the size distribution from the IR emission is more difficult due to the degeneracy between size and ISRF distributions (see Section 2.3.1.2). However, Lisenfeld et al. (2002) and Galliano et al. (2003) attempted the modeling of the IR SED of the dwarf galaxy NGC 1569, varying the size distribution. Both groups concluded that the dust in this object is dominated by nanograins. Interestingly, the extinction curve corresponding to the grain properties found by Galliano et al. (2003) was qualitatively similar to the SMC, with a steep FUV rise and a weak bump. Galliano et al. (2005) found the same result for three other dwarf galaxies. In the LMC, Paradis et al. (2009) also concluded that there is a drastic increase of the fraction of very small grains, especially around 30 Dor. It is possible that, even if a fraction of hot equilibrium dust has been mistaken for small grains by these studies, these systems harbor, on average, smaller grains than normal galaxies. SN-triggered shock waves, which are abundant in star-forming dwarf galaxies (see Section 2.1.3), by fragmenting large grains, could explain the peculiar SEDs and extinction curves of dwarf galaxies (see, e.g., Bocchio et al. 2014, figure 17, $V_{shock} = 100$ km/s).

4.2.3. Grain destruction.
The dust destruction efficiency in SN-triggered shock waves was recently re-estimated using the model of Jones et al. (2017) to evaluate the role of dust mantles and to calculate the emission and extinction from shocked dust (Bocchio et al. 2014). Further constraints were put on the silicate destruction time using hydrodynamical simulations (Slavin et al. 2015). The main conclusions of these studies are as follows: (*a*) a-C(:H) grains are quickly destroyed, even in a 50-km/s shock, which is counter to earlier work (see, e.g., Jones et al. 1996), which used the properties of graphite and an amorphous carbon other than a-C(:H). It implies that the reformation of carbonaceous dust in the dense regions of the ISM is a strong requirement (see Section 4.2.1). (*b*) Silicate grains appear to be more resilient, with a mean lifetime of $\tau_{sil} \simeq 2$–3 Gyr

(Slavin et al. 2015), one order of magnitude larger than the previous estimate of $\tau_{\rm sil} \simeq 400$ Myr (Jones et al. 1996).

4.2.3.1. Photodestruction of small grains. In Galactic PDRs, Boulanger et al. (1998, figure 3) showed that the UIB strength departs from a linear dependence on the ISRF intensity, U, for $U \gtrsim 1,000$, indicating that band carrier destruction has occurred. This implies that, in a galaxy with regions of intense stellar radiation, the observed UIBs are most likely not coming from high-ISRF regions. More recently, work on radiative transfer modeling of the dust emission in Galactic PDRs has shown that small grains are significantly underabundant with respect to the diffuse ISM (Arab et al. 2012).

This phenomenon is widely observed in nearby galaxies. First, the UIB carriers appear to have been cleared out of the hotter parts of extragalactic, star-forming regions (see, e.g., Galametz et al. 2013, Wu et al. 2015). This destruction impacts a larger volume in blue compact galaxies. For example, in NGC 5253, the 11.3-μm equivalent width increases with the distance from the SSC region, over several hundreds of parsecs (Beirão et al. 2006). Second, the $L_{3.3}/L_{\rm IR}$ ratio of LIRGs and ULIRGs decreases when $L_{\rm IR}$ increases (see, e.g., Imanishi et al. 2010). Since $L_{\rm IR}$ quantifies the SFR (Section 2.4.1), this relation indicates that the UIB destruction can be seen at the scale of the whole galaxy. Finally, there are well-known correlations between the UIB equivalent width and various tracers of the intensity and hardness of the radiation field, such as the ionic line ratio [NeIII]$_{15.56\,\mu m}$/[NeII]$_{12.81\,\mu m}$ (Madden et al. 2006, Gordon et al. 2008, Lebouteiller et al. 2011). These correlations are observed both within spatially resolved sources and among integrated galaxies. These results suggest that scaling a diffuse ISM-type dust emission to regions of enhanced radiation field, such as in **Figure 3c**, is not appropriate.

4.2.3.2. Sputtering: grain evolution in hot plasmas. The superwind of M82 exhibits filaments of dust and gas around the central outflows. PAHs or carbonaceous nanoparticles embedded in such energetic regions would be exposed to soft X-rays (0.5–2.0 keV) and a hot gas ($T_{\rm gas} \simeq 10^7$ K; see Section 2.1.5). In such regions, their survival time is only $\simeq 20$ Myr, and their destruction is principally due to collisions with the hot gas rather than X-ray photodestruction (Micelotta et al. 2010). Yet, UIBs are detected in these outflows (see, e.g., Yamagishi et al. 2012, Beirão et al. 2015). Thus, they are likely protected in the entrained cold gas that is being ablated into the hot outflowing gas, rather than being present in the hot gas itself (Micelotta et al. 2010, Bocchio et al. 2012, 2013).

4.3. Cosmic Dust Evolution

The correlation between combinations of global parameters, such as $M_{\rm dust}$, $M_{\rm gas}$, $M_{\rm star}$, and SFR, across galaxy types, provides observational clues of cosmic evolution.

4.3.1. Dust-related scaling relations. Dust-related scaling relations have thrived on *Herschel* data, as this observatory has provided reliable dust mass estimates for statistical samples of galaxies, with various selection criteria (see, e.g., Cortese et al. 2012, Rémy-Ruyer et al. 2015, Clark et al. 2015, De Vis et al. 2017a). **Figure 8a** displays the evolution of the dust-to-gas mass ratio as a function of the specific gas mass. When a galaxy evolves, its gas content is converted into stars, reducing the $M_{\rm gas}/M_{\rm star}$ ratio. At the same time, the ISM is enriched in dust, increasing the $M_{\rm dust}/M_{\rm gas}$ ratio. We also see that early-type galaxies, which are X-ray bright sources, lie noticeably below the correlation. This is possibly the result of thermal sputtering of the grains in a hot plasma ($T \gtrsim 10^6$ K; De Vis et al. 2017a). **Figure 8b** demonstrates the effect of astration on
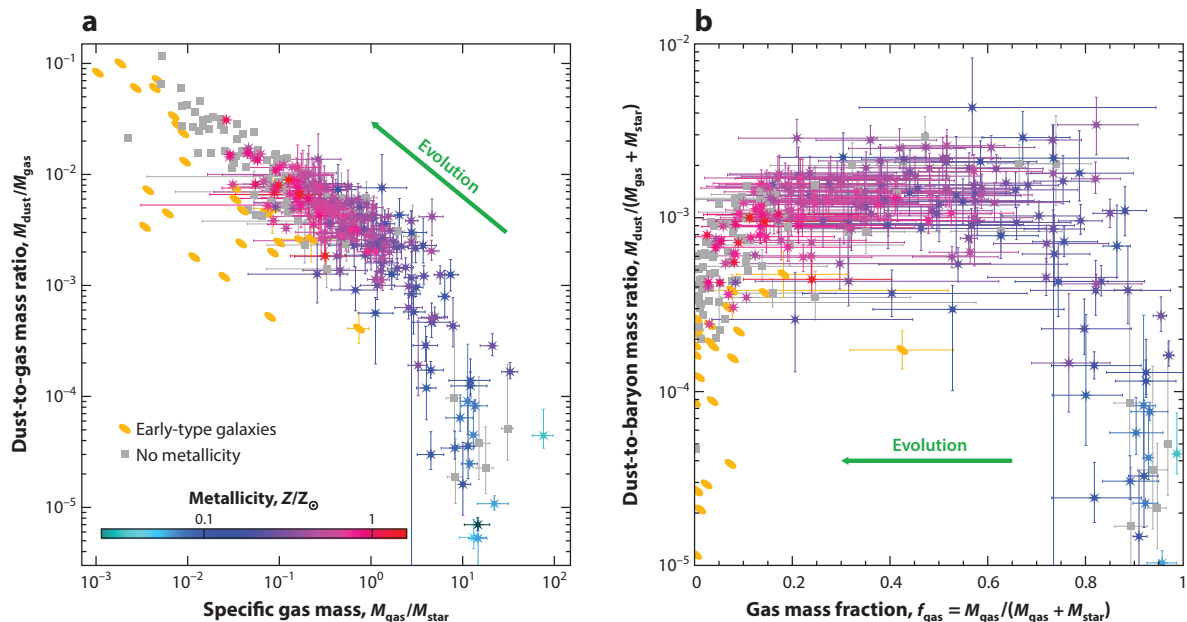
Figure 8

Main scaling relations. Each point represents a nearby galaxy from the volume-limited samples of De Vis et al. (2017a, H I–selected), Clark et al. (2015, 250 μm–selected), Cortese et al. (2012, *K*-band–selected), and Rémy-Ruyer et al. (2015, *Z*-selected), homogenized by De Vis et al. (2017b). In both panels, the galaxies are color coded with metallicity, when this is available. The gas mass is estimated with the sole neutral atomic tracer $M_{gas} \simeq 1.32 M_{HI}$, accounting for He.

the dust content. It shows an early dust buildup ($f_{gas} \gtrsim 0.8$), then a plateau, and then a net mass loss ($f_{gas} \lesssim 0.2$).

4.3.2. Dust-to-gas mass ratio evolution with metallicity. An important scaling relation, often used to constrain dust evolution models, is the trend of dust-to-gas mass ratio with metallicity (see, e.g., Lisenfeld & Ferrara 1998, Draine et al. 2007, Galliano et al. 2008, Rémy-Ruyer et al. 2014, De Vis et al. 2017b). **Figure 9a** shows this relation for nearby galaxies. It is clearly nonlinear, suggesting that dust production is less efficient at early stages. There are several sources of uncertainty that could bias this relation. First, to derive the dust mass, the dust constitution has been assumed to be homogeneous throughout the whole sample. However, the expected variations of the grain mixture constitution (see Section 4.2.1) could alter the dust mass by a factor of $\simeq 2$–3 (Köhler et al. 2015), which is only a minor effect on a trend spanning four orders of magnitude. Second, the estimate of the gas mass could be inaccurate. In particular, the absence of molecular gas mass constraints is problematic. However, we note that Rémy-Ruyer et al. (2014), using CO-derived H_2 masses and exploring the effects of different CO-to-H_2 conversion factors, found a similar trend. As noted by De Vis et al. (2017a), the displayed sample is not H_2-dominated, and the uncertainty on the total gas mass is not expected to be larger than a factor of $\simeq 2$. Third, low-metallicity galaxies usually have large H I halos surrounding their dust-emitting region (see Section 2.1.3). A dust-to-gas mass ratio encompassing the whole halo would therefore be underestimated (see the discussions by Draine et al. 2007, Rémy-Ruyer et al. 2014). This effect has been partially corrected for by Rémy-Ruyer et al. (2014) on the basis of the available H I maps of their sample. In particular, the H I mass
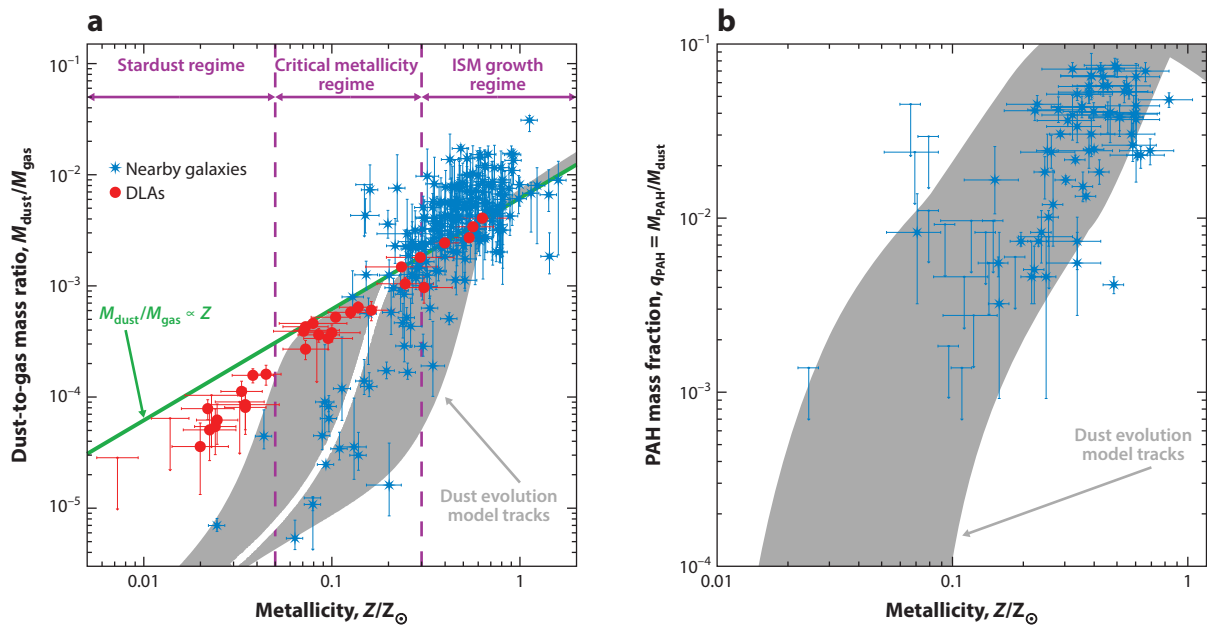
Figure 9

Dust evolution with metallicity. (*a*) Total dust-to-gas mass ratios of nearby galaxies (De Vis et al. 2017b) (*blue*) and DLAs (De Cia et al. 2016) (*red*). The gray area represents the tracks of the model of Asano et al. (2013), varying the star-formation timescale from $\tau_{SF} = 0.5$ to 50 Gyr ($\tau_{SF} = 5$ Gyr, *white curve*). The green line shows the locus of a constant, Galactic dust-to-metal mass ratio. (*b*) PAH-to-dust mass ratios for the nearby galaxy sample of Rémy-Ruyer et al. (2015). The gray area shows the tracks of the Galliano et al. (2008) dust evolution model. The metallicity, Z, has been derived from the O abundance. Abbreviations: DLA, damped Lyα system; ISM, interstellar medium; PAH, polycyclic aromatic hydrocarbon.

of the lowest-metallicity source in **Figure 9*a***, I Zw 18, has been corrected. It is therefore difficult to understand how the nonlinearity of the trend would result solely from measurement biases.

We compare the nearby galaxy trend to the DLA sample of De Cia et al. (2016), in **Figure 9*a***. The dust-to-gas mass ratio and the metallicity of DLAs are all estimated from redshifted UV absorption lines (Section 3.3). These sources show an almost perfectly linear trend down to $\simeq 1/100$ $Z_{\odot}$. Their dust-to-metal mass ratio varies by only a factor of $\simeq 3$ over the whole metallicity range.

4.3.3. Models of global dust evolution. It is possible to model the dust evolution of a galaxy, over cosmic time, by accounting for the balance between the production and destruction mechanisms. This approach was initiated by Dwek & Scalo (1980), who included grain processing in gas enrichment models. The main physical ingredients are the following. First, the star-formation history of the galaxy is the driving mechanism. It can consist of episodic bursts parameterized by different timescales or can be regulated by inflow and outflow rates. Second, when stellar populations are born, depending on their IMF, they will destroy a fraction of the dust by astration. Third, at the end of their lifetime, stars inject newly formed heavy elements and dust into the ISM. The stellar yields of core-collapse SNe and AGB stars are, however, quite uncertain (see the discussion by Matsuura et al. 2015). Fourth, grains grow in the ISM by accretion. However, the associated sticking coefficients are uncertain. Finally, as massive stars die, dust is destroyed

by their SN-triggered shock waves, whose efficiency is also uncertain (see Section 4.2.3). Most studies develop one-zone models. The evolution of the size distribution can be tracked (see, e.g., Hirashita 2015).

Despite the noted uncertainty in the efficiency of the individual processes, these models provide consistent trends of dust-to-gas ratio with metallicity, which inform the observations discussed in Section 4.3.2. We display the area covered by different dust evolution tracks in **Figure 9a**. These tracks correspond to different star-formation histories. They provide a remarkable description of the nearby galaxy distribution. They can be characterized by the three following regimes. First, at low Z, the grains are mainly condensed in stellar ejecta, and the dust-to-gas ratio is proportional to metallicity but with a low dust-to-metal ratio. Second, at intermediate metallicities, grain growth in the ISM starts to become important, as there are more heavy elements to be accreted. The overall dust production efficiency increases. Third, at metallicity close to solar, we reach a linear regime dominated by grain growth. The nearby galaxy trend in **Figure 9a** therefore suggests that grain growth is a crucial process (see also Section 4.2.3). The scattering among the different objects can be explained by different star-formation histories. By contrast, the DLA trend does not seem to agree with the displayed dust evolution models. This disagreement is currently debated. It might be due to the particular history of these systems. For example, it is possible to have a quasi-linear trend, down to low Z, with an episodic star-formation history (Zhukovska 2014).

4.3.4. Aromatic feature strength evolution with metallicity.
The UIB equivalent width clearly rises with metallicity. This was first demonstrated by Engelbracht et al. (2005), using broadband photometry, and by Madden et al. (2006), using spectroscopic observations. Engelbracht et al. (2005) argued that there were two regimes: a high UIB fraction above $\simeq 1/5$–$1/3$ $Z_\odot$ and a low value below this range. However, Galliano et al. (2008) demonstrated that this was a bias resulting from the fact that the continuum dominates the MIR broadbands when the UIB strength becomes weak. Trends constrained with spectroscopy appear rather smooth, although there is significant scatter (**Figure 9b**). It was rapidly proposed that the origin of this phenomenon was the enhanced destruction of the UIB carriers in the UV-permeated ISM of dwarf galaxies (see Section 4.2.3.1), illustrating again the degeneracy between star-formation activity and metallicity (see Section 4.1). Indeed, the UIB strength appears slightly better correlated with tracers of the ISRF hardness than with the metallicity (see, e.g., Gordon et al. 2008, Wu et al. 2011).

UIB carrier destruction is indubitably an important process in low-Z systems, but it does not exclude the possible deficiency of their formation. Galliano et al. (2008) hypothesized that UIB carriers could be mostly produced by long-lived AGB stars. This delayed injection mechanism could explain the trend (**Figure 9b**). However, as we have seen in Section 4.2.3, UIB carriers are very volatile and need to re-form in the ISM. Alternatively, Seok et al. (2014) showed that a dust evolution model in which PAHs are formed by fragmentation of large carbonaceous grains can explain the observed PAH trend. Observationally, Sandstrom et al. (2010), modeling the MIR spectra of several regions in the SMC, found that the PAH mass fraction correlates better with the molecular gas. They proposed that PAHs could form in molecular clouds. The trend with the metallicity would then result from the lower filling factor of the molecular gas at low Z. This interesting scenario is probably not complete, as the PAH fractions they found in shielded regions are still a factor of $\simeq 2$–4 lower than in the MW. This is not surprising, as the C/O ratio is about half of that in the SMC (**Table 2**). There is no simple answer to this open question, but it appears that, to explain the paucity of UIBs in low-Z environments, one needs to invoke both their photodestruction and the deficiency of their formation process.

FUTURE ISSUES

1. Current dust models do not provide a parameterization of the grain mixture constitution as a function of the physical conditions. As we have discussed, local evolution processes, such as the photodestruction of small grains and mantle growth and evaporation, bias our interpretations when we use models with a fixed constitution. Working toward being able to predict, even in a simplified way, the grain properties for an arbitrary gas density and ISRF intensity is necessary to interpret already existing observations.

2. We are now at a time when nearby galaxies have been observed in detail over the whole electromagnetic spectrum. We are thus compelled to think beyond integrated broadband fluxes to achieve further progress. (*a*) Spatially resolved studies ($\lesssim 1$ arcsec) are possible in the MIR range with JWST and in the submillimeter range with *ALMA*. These could help resolve the dust heating in dense extragalactic PDRs (Equation 2) and thus provide constraints on the dust properties in high-ISRF conditions. (*b*) FIR spectroscopy (SPICA) would be valuable for better constraining the shape of the SED and for identifying new solid-state features. (*c*) Multiprocess studies are the key to solving the degeneracies inherent to dust models. LUVOIR could provide valuable constraints on the extinction, depletion, DIBs, and ERE of regions or galaxies that have been observed with the previous IR–submm telescopes.

3. The increase in sensitivity of the next generation of instruments will be a challenge for data analysis methods. More precise fluxes will require proper accounts of foreground and background emissions, especially if we are interested in the diffuse ISM of galaxies. More complex spatial and spectral decomposition methods, with rigorous treatment of the uncertainties, will be necessary.

JWST: *James Webb Space Telescope*; NIR–MIR space telescope ($\lambda \simeq 0.6$–27 μm; launch in 2021) with subarcsec resolution

SPICA: *Space Infrared Telescope for Cosmology and Astrophysics*; MIR–FIR space telescope ($\lambda \simeq 12$–210 μm; launch in ∼2025) with unprecedented sensitivity

LUVOIR: *Large UV/Optical/IR Surveyor*; UV–NIR space telescope (in preparation)

DISCLOSURE STATEMENT

The authors are not aware of any affiliations, memberships, funding, or financial holdings that might be perceived as affecting the objectivity of this review.

ACKNOWLEDGMENTS

LITERATURE CITED

Allamandola LJ, Tielens AGGM, Barker JR. 1985. *Ap. J.* 290:L25–28
Aloisi A, Savaglio S, Heckman TM, et al. 2003. *Ap. J.* 595:760–78

Alton PB, Draper PW, Gledhill TM, et al. 1994. *MNRAS* 270:238

Alton PB, Trewhella M, Davies JI, et al. 1998. *Astron. Astrophys.* 335:807–22

Alton PB, Xilouris EM, Bianchi S, Davies J, Kylafis N. 2000. *Astron. Astrophys.* 356:795–807

Alton PB, Xilouris EM, Misiriotis A, Dasyra KM, Dumke M. 2004. *Astron. Astrophys.* 425:109–20

Amanullah R, Goobar A, Johansson J, et al. 2014. *Ap. J.* 788:L21

Aniano G, Draine BT, Calzetti D, et al. 2012. *Ap. J.* 756:138

Antonucci R. 1993. *Annu. Rev. Astron. Astrophys.* 31:473–521

Antonucci RRJ, Miller JS. 1985. *Ap. J.* 297:621–32

Arab H, Abergel A, Habart E, et al. 2012. *Astron. Astrophys.* 541:A19

Asano RS, Takeuchi TT, Hirashita H, Inoue AK. 2013. *Earth Planets Space* 65:213–22

Baes M, Davies JI, Dejonghe H, et al. 2003. *MNRAS* 343:1081–94

Baes M, Fritz J, Gadotti DA, et al. 2010. *Astron. Astrophys.* 518:L39

Bailey M, van Loon JT, Sarre PJ, Beckman JE. 2015. *MNRAS* 454:4013–26

Battisti AJ, Calzetti D, Chary RR. 2016. *Ap. J.* 818:13

Beirão P, Armus L, Lehnert MD, et al. 2015. *MNRAS* 451:2640–55

Beirão P, Brandl BR, Devost D, et al. 2006. *Ap. J.* 643:L1–4

Bendo GJ, Boselli A, Dariush A, et al. 2012. *MNRAS* 419:1833–59

Bendo GJ, Dale DA, Draine BT, et al. 2006. *Ap. J.* 652:283–305

Bendo GJ, Draine BT, Engelbracht CW, et al. 2008. *MNRAS* 389:629–50

Bendo GJ, Joseph RD, Wells M, et al. 2002. *Astron. J.* 123:3067–107

Bendo GJ, Wilson CD, Pohlen M, et al. 2010. *Astron. Astrophys.* 518:L65

Berlind AA, Quillen AC, Pogge RW, Sellgren K. 1997. *Astron. J.* 114:107–14

Bianchi L, Clayton GC, Bohlin RC, Hutchings JB, Massey P. 1996. *Ap. J.* 471:203

Bianchi S. 2007. *Astron. Astrophys.* 471:765–73

Bianchi S. 2008. *Astron. Astrophys.* 490:461–75

Block DL, Puerari I, Elmegreen BG, Bournaud F. 2010. *Ap. J.* 718:L1–6

Block DL, Witt AN, Grosbol P, Stockton A, Moneti A. 1994. *Astron. Astrophys.* 288:383–95

Bocchio M, Bianchi S, Hunt LK, Schneider R. 2016. *Astron. Astrophys.* 586:A8

Bocchio M, Jones AP, Slavin JD. 2014. *Astron. Astrophys.* 570:A32

Bocchio M, Jones AP, Verstraete L, et al. 2013. *Astron. Astrophys.* 556:A6

Bocchio M, Micelotta ER, Gautier AL, Jones AP. 2012. *Astron. Astrophys.* 545:A124

Bolte M, Saddlemyer L, Mendes de Oliveira C, Hodder P. 1989. *Publ. Astron. Soc. Pac.* 101:921–24

Boquien M, Calzetti D, Combes F, et al. 2011. *Astron. J.* 142:111

Boquien M, Duc PA, Galliano F, et al. 2010. *Astron. J.* 140:2124–44

Boquien M, Kennicutt R, Calzetti D, et al. 2016. *Astron. Astrophys.* 591:A6

Boselli A, Ciesla L, Buat V, et al. 2010. *Astron. Astrophys.* 518:L61

Boselli A, Ciesla L, Cortese L, et al. 2012. *Astron. Astrophys.* 540:A54

Boselli A, Sauvage M, Lequeux J, Donati A, Gavazzi G. 2003. *Astron. Astrophys.* 406:867–77

Bot C, Ysard N, Paradis D, et al. 2010. *Astron. Astrophys.* 523:A20

Boudet N, Mutschke H, Nayral C, et al. 2005. *Ap. J.* 633:272–81

Boulanger F, Abergel A, Bernard JP, et al. 1998. The nature of small interstellar dust particles. In *Star Formation with the Infrared Space Observatory*, ed. J Yun, L Liseau, pp. 15–23. San Francisco: Astron. Soc. Pac.

Boulanger F, Perault M. 1988. *Ap. J.* 330:964–85

Bressan A, Panuzzo P, Buson L, et al. 2006. *Ap. J.* 639:L55–L58

Calzetti D. 2001. *Publ. Astron. Soc. Pac.* 113:1449–85

Calzetti D, Armus L, Bohlin RC, et al. 2000. *Ap. J.* 533:682–95

Calzetti D, Kennicutt RC, Engelbracht CW, et al. 2007. *Ap. J.* 666:870–95

Calzetti D, Kinney AL, Storchi-Bergmann T. 1994. *Ap. J.* 429:582–601

Campbell EK, Holz M, Gerlich D, Maier JP. 2015. *Nature* 523:322–23

Cardelli JA, Clayton GC, Mathis JS. 1989. *Ap. J.* 345:245–56

Cartledge SIB, Clayton GC, Gordon KD, et al. 2005. *Ap. J.* 630:355–67

Chevance M, Madden SC, Lebouteiller V, et al. 2016. *Astron. Astrophys.* 590:A36

Clark CJR, Dunne L, Gomez HL, et al. 2015. *MNRAS* 452:397–430

Clayton GC, Gordon KD, Bianchi LC, et al. 2015. *Ap. J.* 815:14
Clayton GC, Gordon KD, Salama F, et al. 2003. *Ap. J.* 592:947–52
Clayton GC, Green J, Wolff MJ, et al. 1996. *Ap. J.* 460:313
Clayton GC, Wolff MJ, Gordon KD, et al. 2004. *Astron. J.* 127:3382–87
Clements DL, Sutherland WJ, McMahon RG, Saunders W. 1996. *MNRAS* 279:477–97
Cole AA, Nordsieck KH, Gibson SJ, Harris WM. 1999. *Astron. J.* 118:2280–91
Combes F, Boquien M, Kramer C, et al. 2012. *Astron. Astrophys.* 539:A67
Conroy C, Schiminovich D, Blanton MR. 2010. *Ap. J.* 718:184–98
Contursi A, Poglitsch A, Grácia Carpio J, et al. 2013. *Astron. Astrophys.* 549:A118
Cordiner MA, Cox NLJ, Evans CJ, et al. 2011. *Ap. J.* 726:39
Cordiner MA, Smith KT, Cox NLJ, et al. 2008. *Astron. Astrophys.* 492:L5–L8
Cormier D, Madden SC, Lebouteiller V, et al. 2015. *Astron. Astrophys.* 578:A53
Corrales LR, Paerels F. 2015. *MNRAS* 453:1121–35
Cortese L, Ciesla L, Boselli A, et al. 2012. *Astron. Astrophys.* 540:A52
Cox NLJ, Cordiner MA, Cami J, et al. 2006. *Astron. Astrophys.* 447:991–1009
Cox NLJ, Cordiner MA, Ehrenfreund P, et al. 2007. *Astron. Astrophys.* 470:941–55
Cox NLJ, Patat F. 2008. *Astron. Astrophys.* 485:L9–L12
Crenshaw DM, Kraemer SB, Bruhweiler FC, Ruiz JR. 2001. *Ap. J.* 555:633–40
Crinklaw G, Federman SR, Joseph CL. 1994. *Ap. J.* 424:748–53
Crocker AF, Calzetti D, Thilker DA, et al. 2013. *Ap. J.* 762:79
Croxall KV, Smith JD, Wolfire MG, et al. 2012. *Ap. J.* 747:81
da Cunha E, Charlot S, Elbaz D. 2008. *MNRAS* 388:1595–617
Dalcanton JJ, Fouesneau M, Hogg DW, et al. 2015. *Ap. J.* 814:3
Dale DA, Cook DO, Roussel H, et al. 2017. *Ap. J.* 837:90
Dale DA, Helou G, Contursi A, Silbermann NA, Kolhatkar S. 2001. *Ap. J.* 549:215–27
Darbon S, Perrin JM, Sivan JP. 1998. *Astron. Astrophys.* 333:264–68
Dasyra KM, Xilouris EM, Misiriotis A, Kylafis ND. 2005. *Astron. Astrophys.* 437:447–56
Davies JI, Alton P, Trewhella M, Evans R, Bianchi S. 1999. *MNRAS* 304:495–500
Davies JI, Trewhella M, Jones H, et al. 1997. *MNRAS* 288:679–90
Davis L Jr., Greenstein JL. 1951. *Ap. J.* 114:206
De Cia A, Ledoux C, Mattsson L, et al. 2016. *Astron. Astrophys.* 596:A97
De Geyter G, Baes M, De Looze I, et al. 2015. *MNRAS* 451:1728–39
De Looze I, Baes M, Bendo GJ, et al. 2012a. *MNRAS* 427:2797–811
De Looze I, Baes M, Fritz J, Verstappen J. 2012b. *MNRAS* 419:895–903
De Marchi G, Panagia N. 2014. *MNRAS* 445:93–106
De Vis P, Dunne L, Maddox S, et al. 2017a. *MNRAS* 464:4680–705
De Vis P, Gomez HL, Schofield SP, et al. 2017b. *MNRAS* 471:1743–65
Deshmukh SP, Tate BT, Vagshette ND, Pandey SK, Patil MK. 2013. *Res. Astron. Astrophys.* 13:885–98
Devereux NA, Young JS. 1990. *Ap. J.* 359:42–56
Dewangan GC, Singh KP, Bhat PN. 1999. *Astron. J.* 118:785–96
Dietz RD, Gehrz RD, Jones TJ, et al. 1989. *Astron. J.* 98:1260–64
Disney M, Davies J, Phillipps S. 1989. *MNRAS* 239:939–76
Dobashi K, Bernard JP, Hughes A, et al. 2008. *Astron. Astrophys.* 484:205–23
D'Odorico S, di Serego Alighieri S, Pettini M, et al. 1989. *Astron. Astrophys.* 215:21–32
Dolginov AZ, Mitrofanov IG. 1976. *Astrophys. Space Sci.* 43:291–317
Dong H, Li Z, Wang QD, et al. 2014. *Ap. J.* 785:136
Draine BT. 1978. *Ap. J. Suppl.* 36:595–619
Draine BT, Anderson N. 1985. *Ap. J.* 292:494–99
Draine BT, Aniano G, Krause O, et al. 2014. *Ap. J.* 780:172
Draine BT, Bond NA. 2004. *Ap. J.* 617:987–1003
Draine BT, Dale DA, Bendo G, et al. 2007. *Ap. J.* 663:866–94
Draine BT, Hensley B. 2012. *Ap. J.* 757:103
Draine BT, Lazarian A. 1998. *Ap. J.* 494:L19

Draine BT, Li A. 2007. *Ap. J.* 657:810–37

Duley WW, Williams DA. 1981. *MNRAS* 196:269–74

Dumke M, Krause M, Wielebinski R. 2004. *Astron. Astrophys.* 414:475–86

Dwek E, Arendt RG, Bouchet P, et al. 2010. *Ap. J.* 722:425–34

Dwek E, Scalo JM. 1980. *Ap. J.* 239:193–211

Elias-Rosa N, Benetti S, Cappellaro E, et al. 2006. *MNRAS* 369:1880–900

Engelbracht CW, Gordon KD, Rieke GH, et al. 2005. *Ap. J.* 628:L29–L32

Evans PA, Willingale R, Osborne JP, et al. 2014. *MNRAS* 444:250–67

Fendt C, Beck R, Neininger N. 1998. *Astron. Astrophys.* 335:123–33

Finkelman I, Brosch N, Kniazev AY, et al. 2010. *MNRAS* 409:727–36

Fitzpatrick EL. 1999. *Publ. Astron. Soc. Pac.* 111:63–75

Fitzpatrick EL, Massa D. 2005. *Astron. J.* 130:1127–40

Friis M, De Cia A, Krühler T, et al. 2015. *MNRAS* 451:167–83

Fukui Y, Torii K, Onishi T, et al. 2015. *Ap. J.* 798:6

Galametz M, Hony S, Galliano F, et al. 2013. *MNRAS* 431:1596–617

Galametz M, Kennicutt RC, Albrecht M, et al. 2012. *MNRAS* 425:763–87

Galametz M, Madden S, Galliano F, et al. 2009. *Astron. Astrophys.* 508:645–64

Galliano F. 2018. *MNRAS* 476:1445–69

Galliano F, Dwek E, Chanial P. 2008. *Ap. J.* 672:214–43

Galliano F, Hony S, Bernard JP, et al. 2011. *Astron. Astrophys.* 536:A88

Galliano F, Madden SC, Jones AP, Wilson CD, Bernard JP. 2005. *Astron. Astrophys.* 434:867–85

Galliano F, Madden SC, Jones AP, et al. 2003. *Astron. Astrophys.* 407:159–76

Galliano F, Madden SC, Tielens AGGM, Peeters E, Jones AP. 2008. *Ap. J.* 679:310–45

Gao J, Jiang BW, Li A, Xue MY. 2013. *Ap. J.* 776:7

Gillett FC, Forrest WJ, Merrill KM. 1973. *Ap. J.* 183:87–93

Gordon KD, Clayton GC, Misselt KA, Landolt AU, Wolff MJ. 2003. *Ap. J.* 594:279–93

Gordon KD, Clayton GC, Witt AN, Misselt KA. 2000. *Ap. J.* 533:236–44

Gordon KD, Engelbracht CW, Rieke GH, et al. 2008. *Ap. J.* 682:336–54

Goudfrooij P, de Jong T. 1995. *Astron. Astrophys.* 298:784

Goudfrooij P, de Jong T, Hansen L, Norgaard-Nielsen HU. 1994. *MNRAS* 271:833

Gould RJ, Salpeter EE. 1963. *Ap. J.* 138:393

Greaves JS, Holland WS, Jenness T, Hawarden TG. 2000. *Nature* 404:732–33

Guillet V, Fanciullo L, Verstraete L, et al. 2018. *Astron. Astrophys.* 610:A16

Guseva NG, Izotov YI, Fricke KJ, Henkel C. 2013. *Astron. Astrophys.* 555:A90

Haas M, Lemke D, Stickel M, et al. 1998. *Astron. Astrophys.* 338:L33–L36

Hall JS. 1949. *Science* 109:166–67

Hao CN, Kennicutt RC, Johnson BD, et al. 2011. *Ap. J.* 741:124

Heckman TM, Lehnert MD. 2000. *Ap. J.* 537:690–96

Heger ML. 1922. *Lick Obs. Bull.* 10:141–45

Helou G, Malhotra S, Hollenbach DJ, Dale DA, Contursi A. 2001. *Ap. J.* 548:L73–76

Hemachandra D, Barmby P, Peeters E, et al. 2015. *MNRAS* 454:818–30

Hensley B, Murphy E, Staguhn J. 2015. *MNRAS* 449:809–19

Hensley BS, Draine BT, Meisner AM. 2016. *Ap. J.* 827:45

Herbig GH. 1995. *Annu. Rev. Astron. Astrophys.* 33:19–74

Hildebrand RH. 1983. *QJRAS* 24:267

Hill RS, Cheng KP, Bohlin RC, et al. 1995. *Ap. J.* 446:622

Hiltner WA. 1949. *Science* 109:165

Hinz JL, Engelbracht CW, Skibba R, et al. 2012. *Ap. J.* 756:75

Hippelein H, Haas M, Tuffs RJ, et al. 2003. *Astron. Astrophys.* 407:137–46

Hirashita H. 2015. *MNRAS* 447:2937–50

Hobbs LM, York DG, Thorburn JA, et al. 2009. *Ap. J.* 705:32–45

Hony S, Kemper F, Woods PM, et al. 2011. *Astron. Astrophys.* 531:A137

Hony S, Van Kerckhoven C, Peeters E, et al. 2001. *Astron. Astrophys.* 370:1030–43

Hopkins PF, Quataert E, Murray N. 2012. *MNRAS* 421:3522–37

Houck JR, Charmandaris V, Brandl BR, et al. 2004. *Ap. J. Suppl.* 154:211–14

Huang X, Raha Z, Aldering G, et al. 2017. *Ap. J.* 836:157

Huchtmeier WK, Seiradakis JH, Materne J. 1981. *Astron. Astrophys.* 102:134–41

Hunt LK, Draine BT, Bianchi S, et al. 2015. *Astron. Astrophys.* 576:A33

Hunt LK, Giovanardi C. 1992. *Astron. J.* 104:1018–38

Hunt LK, Thuan TX, Izotov YI, Sauvage M. 2010. *Ap. J.* 712:164–87

Hunter DA, Elmegreen BG, Martin E. 2006. *Astron. J.* 132:801–18

Hutton S, Ferreras I, Yershov V. 2015. *MNRAS* 452:1412–20

Imanishi M, Nakagawa T, Shirahata M, Ohyama Y, Onaka T. 2010. *Ap. J.* 721:1233–61

Israel FP. 1997. *Astron. Astrophys.* 328:471–82

Israel FP, Wall WF, Raban D, et al. 2010. *Astron. Astrophys.* 519:A67

Izotov YI, Stasińska G, Meynet G, Guseva NG, Thuan TX. 2006. *Astron. Astrophys.* 448:955–70

James BL, Aloisi A, Heckman T, Sohn ST, Wolfe MA. 2014. *Ap. J.* 795:109

Jenkins EB. 2009. *Ap. J.* 700:1299–348

Jenkins EB, Wallerstein G. 2017. *Ap. J.* 838:85

Jones AG, Bendo GJ, Baes M, et al. 2015. *MNRAS* 448:168–87

Jones AP, Fanciullo L, Köhler M, et al. 2013. *Astron. Astrophys.* 558:A62

Jones AP, Köhler M, Ysard N, Bocchio M, Verstraete L. 2017. *Astron. Astrophys.* 602:A46

Jones AP, Tielens AGGM, Hollenbach DJ. 1996. *Ap. J.* 469:740

Jones TJ. 2000. *Astron. J.* 120:2920–27

Joseph RD, Meikle WPS, Robertson NA, Wright GS. 1984. *MNRAS* 209:111–22

Jura M, Kim DW, Knapp GR, Guhathakurta P. 1987. *Ap. J.* 312:L11–L15

Juvela M, Ysard N. 2012. *Astron. Astrophys.* 539:A71

Kaneda H, Onaka T, Sakon I. 2007. *Ap. J.* 666:L21–L24

Kapala MJ, Groves B, Sandstrom K, et al. 2017. *Ap. J.* 842:128

Kawabata KS, Akitaya H, Yamanaka M, et al. 2014. *Ap. J.* 795:L4

Kelly BC, Shetty R, Stutz AM, et al. 2012. *Ap. J.* 752:55

Kemper F, Vriend WJ, Tielens AGGM. 2004. *Ap. J.* 609:826–37

Kogut A, Banday AJ, Bennett CL, et al. 1996. *Ap. J.* 464:L5

Köhler M, Ysard N, Jones AP. 2015. *Astron. Astrophys.* 579:A15

Kondo T, Kaneda H, Oyabu S, et al. 2012. *Ap. J.* 751:L18

Korn AJ, Keller SC, Kaufer A, et al. 2002. *Astron. Astrophys.* 385:143–51

Lan TW, Ménard B, Zhu G. 2015. *MNRAS* 452:3629–49

Lawton B, Churchill CW, York BA, et al. 2008. *Astron. J.* 136:994–1012

Le Petit F, Nehmé C, Le Bourlot J, Roueff E. 2006. *Ap. J. Suppl.* 164:506–29

Lebouteiller V, Barry DJ, Spoon HWW, et al. 2011. *Ap. J. Suppl.* 196:8

Lebouteiller V, Heap S, Hubeny I, Kunth D. 2013. *Astron. Astrophys.* 553:A16

Lebouteiller V, Péquignot D, Cormier D, et al. 2017. *Astron. Astrophys.* 602:A45

Lee JC, Xiang J, Ravel B, Kortright J, Flanagan K. 2009. *Ap. J.* 702:970–79

Léger A, Puget JL. 1984. *Astron. Astrophys.* 137:L5–L8

Leroy AK, Bolatto A, Gordon K, et al. 2011. *Ap. J.* 737:12

Li A, Greenberg JM. 2002. *Ap. J.* 577:789–94

Li Y, Calzetti D, Kennicutt RC, et al. 2010. *Ap. J.* 725:677–91

Lisenfeld U, Ferrara A. 1998. *Ap. J.* 496:145

Lisenfeld U, Israel FP, Stil JM, Sievers A. 2002. *Astron. Astrophys.* 382:860–71

Lobo Gomes A, Magalhães AM, Pereyra A, Rodrigues CV. 2015. *Ap. J.* 806:94

Lonsdale Persson CJ, Helou G. 1987. *Ap. J.* 314:513–24

Lu N, Helou G, Werner MW, et al. 2003. *Ap. J.* 588:199–217

Lutz D, Feuchtgruber H, Genzel R, et al. 1996. *Astron. Astrophys.* 315:L269–72

Madden SC, Galliano F, Jones AP, Sauvage M. 2006. *Astron. Astrophys.* 446:877–96

Madden SC, Poglitsch A, Geis N, Stacey GJ, Townes CH. 1997. *Ap. J.* 483:200

Maiolino R, Marconi A, Salvati M, et al. 2001. *Astron. Astrophys.* 365:28–36

Malhotra S, Helou G, van Buren D, et al. 1996. *Astron. Astrophys.* 315:L161–64

Mallouris C. 2003. *Ap. J. Suppl.* 147:265–303

Mason RE, Wright GS, Adamson A, Pendleton Y. 2007. *Ap. J.* 656:798–804

Matsuura M, Dwek E, Barlow MJ, et al. 2015. *Ap. J.* 800:50

Meijerink R, Tilanus RPJ, Dullemond CP, Israel FP, van der Werf PP. 2005. *Astron. Astrophys.* 430:427–34

Melisse JPM, Israel FP. 1994. *Astron. Astrophys.* 285:51–68

Mennella V, Brucato JR, Colangeli L, et al. 1998. *Ap. J.* 496:1058

Mentuch E, Abraham RG, Zibetti S. 2010. *Ap. J.* 725:1971–83

Meny C, Gromov V, Boudet N, et al. 2007. *Astron. Astrophys.* 468:171–88

Micelotta ER, Jones AP, Tielens AGGM. 2010. *Astron. Astrophys.* 510:A37

Montgomery JD, Clemens DP. 2014. *Ap. J.* 786:41

Mori TI, Sakon I, Onaka T, et al. 2012. *Ap. J.* 744:68

Muñoz-Mateos JC, Gil de Paz A, Boissier S, et al. 2009a. *Ap. J.* 701:1965–91

Muñoz-Mateos JC, Gil de Paz A, Zamorano J, et al. 2009b. *Ap. J.* 703:1569–96

Murphy EJ, Helou G, Condon JJ, et al. 2010. *Ap. J.* 709:L108–13

Nandy K, Morgan DH, Willis AJ, Wilson R, Gondhalekar PM. 1981. *MNRAS* 196:955–66

Oey MS. 1996. *Ap. J.* 467:666

Oliveira JM, van Loon JT, Sloan GC, et al. 2013. *MNRAS* 428:3001–33

Onaka T, Matsumoto H, Sakon I, Kaneda H. 2010. *Astron. Astrophys.* 514:A15

Padoan P, Kim S, Goodman A, Staveley-Smith L. 2001. *Ap. J.* 555:L33–L36

Paradis D, Paladini R, Noriega-Crespo A, et al. 2012. *Astron. Astrophys.* 537:A113

Paradis D, Reach WT, Bernard J, et al. 2009. *Astron. J.* 138:196–209

Patat F, Taubenberger S, Cox NLJ, et al. 2015. *Astron. Astrophys.* 577:A53

Peña-Guerrero MA, Peimbert A, Peimbert M, Ruiz MT. 2012. *Ap. J.* 746:115

Peel MW, Dickinson C, Davies RD, Clements DL, Beswick RJ. 2011. *MNRAS* 416:L99–L103

Peeters E, Martín-Hernández NL, Damour F, et al. 2002. *Astron. Astrophys.* 381:571–605

Peeters E, Spoon HWW, Tielens AGGM. 2004. *Ap. J.* 613:986–1003

Perrin JM, Darbon S, Sivan JP. 1995. *Astron. Astrophys.* 304:L21

Phillips MM, Phillips AC, Heathcote SR, et al. 1987. *Publ. Astron. Soc. Pac.* 99:592–605

Pierini D, Gordon KD, Witt AN, Madsen GJ. 2004. *Ap. J.* 617:1022–46

Pierini D, Majeed A, Boroson TA, Witt AN. 2002. *Ap. J.* 569:184–203

Planck Collaboration. 2011a. *Astron. Astrophys.* 536:A17

Planck Collaboration. 2011b. *Astron. Astrophys.* 536:A20

Planck Collaboration. 2014. *Astron. Astrophys.* 571:A11

Planck Collaboration. 2015a. *Astron. Astrophys.* 576:A105

Planck Collaboration. 2015b. *Astron. Astrophys.* 582:A28

Planck Collaboration. 2016. *Astron. Astrophys.* 586:A132

Poglitsch A, Krabbe A, Madden SC, et al. 1995. *Ap. J.* 454:293

Popescu CC, Tuffs RJ. 2003. *Astron. Astrophys.* 410:L21–24

Popescu CC, Tuffs RJ, Dopita MA, et al. 2011. *Astron. Astrophys.* 527:A109

Reach WT, Boulanger F, Contursi A, Lequeux J. 2000. *Astron. Astrophys.* 361:895–900

Reach WT, Dwek E, Fixsen DJ, et al. 1995. *Ap. J.* 451:188

Reines AE, Johnson KE, Goss WM. 2008a. *Astron. J.* 135:2222–39

Reines AE, Johnson KE, Hunt LK. 2008b. *Astron. J.* 136:1415–26

Reines AE, Nidever DL, Whelan DG, Johnson KE. 2010. *Ap. J.* 708:26–37

Rémy-Ruyer A, Madden SC, Galliano F, et al. 2013. *Astron. Astrophys.* 557:A95

Rémy-Ruyer A, Madden SC, Galliano F, et al. 2014. *Astron. Astrophys.* 563:A31

Rémy-Ruyer A, Madden SC, Galliano F, et al. 2015. *Astron. Astrophys.* 582:A121

Ritchey AM, Wallerstein G. 2015. *Publ. Astron. Soc. Pac.* 127:223

Rodrigues CV, Magalhães AM, Coyne GV, Piirola SJV. 1997. *Ap. J.* 485:618–37

Rodríguez-Ardila A, Contini M, Viegas SM. 2005. *MNRAS* 357:220–34

Roman-Duval J, Bot C, Chastenet J, Gordon K. 2017. *Ap. J.* 841:72

Roman-Duval J, Gordon KD, Meixner M, et al. 2014. *Ap. J.* 797:86

Rosa MR, Benvenuti P. 1994. *Astron. Astrophys.* 291:1–17

Roth KC, Blades JC. 1997. *Ap. J.* 474:L95–L98

Roussel H, Vigroux L, Bosma A, et al. 2001. *Astron. Astrophys.* 369:473–509

Rubin D, Hony S, Madden SC, et al. 2009. *Astron. Astrophys.* 494:647–61

Sadler EM, Gerhard OE. 1985. *MNRAS* 214:177–87

Sales DA, Pastoriza MG, Riffel R. 2010. *Ap. J.* 725:605–14

Sandford SA, Bernstein MP, Materese CK. 2013. *Ap. J. Suppl.* 205:8

Sandstrom KM, Bolatto AD, Bot C, et al. 2012. *Ap. J.* 744:20

Sandstrom KM, Bolatto AD, Draine BT, Bot C, Stanimirović S. 2010. *Ap. J.* 715:701–23

Sauvage M, Blommaert J, Boulanger F, et al. 1996. *Astron. Astrophys.* 315:L89–L92

Savage BD, Bohlin RC. 1979. *Ap. J.* 229:136–46

Savage BD, Sembach KR. 1996. *Annu. Rev. Astron. Astrophys.* 34:279–330

Scaife AMM, Nikolic B, Green DA, et al. 2010. *MNRAS* 406:L45–L49

Scarrott SM, Foley NB, Gledhill TM, Wolstencroft RD. 1996. *MNRAS* 282:252–62

Sellgren K. 1984. *Ap. J.* 277:623–33

Sembach KR, Howk JC, Savage BD, Shull JM. 2001. *Astron. J.* 121:992–1002

Seok JY, Hirashita H, Asano RS. 2014. *MNRAS* 439:2186–96

Serkowski K, Mathewson DS, Ford VL. 1975. *Ap. J.* 196:261–90

Shetty R, Kauffmann J, Schnee S, Goodman AA. 2009. *Ap. J.* 696:676–80

Slavin JD, Dwek E, Jones AP. 2015. *Ap. J.* 803:7

Smith BJ, Hancock M. 2009. *Astron. J.* 138:130–45

Smith JDT, Croxall K, Draine B, et al. 2017. *Ap. J.* 834:5

Smith JDT, Draine BT, Dale DA, et al. 2007. *Ap. J.* 656:770–91

Smith MWL, Gomez HL, Eales SA, et al. 2012. *Ap. J.* 748:123

Smith RK, Valencic LA, Corrales L. 2016. *Ap. J.* 818:143

Sofia UJ, Gordon KD, Clayton GC, et al. 2006. *Ap. J.* 636:753–64

Sollerman J, Cox N, Mattila S, et al. 2005. *Astron. Astrophys.* 429:559–67

Spoon HWW, Tielens AGGM, Armus L, et al. 2006. *Ap. J.* 638:759–65

Stecher TP. 1965. *Ap. J.* 142:1683

Stein W. 1966. *Ap. J.* 144:318

Stepnik B, Abergel A, Bernard J, et al. 2003. *Astron. Astrophys.* 398:551–63

Stevens JA, Amure M, Gear WK. 2005. *MNRAS* 357:361–80

Stierwalt S, Armus L, Charmandaris V, et al. 2014. *Ap. J.* 790:124

Tabatabaei FS, Braine J, Xilouris EM, et al. 2014. *Astron. Astrophys.* 561:A95

Tchernyshyov K, Meixner M, Seale J, et al. 2015. *Ap. J.* 811:78

Tempel E, Tamm A, Tenjes P. 2010. *Astron. Astrophys.* 509:A91

Thorburn JA, Hobbs LM, McCall BJ, et al. 2003. *Ap. J.* 584:339–56

Thuan TX, Sauvage M, Madden S. 1999. *Ap. J.* 516:783–87

Trewhella M, Davies JI, Alton PB, Bianchi S, Madore BF. 2000. *Ap. J.* 543:153–60

Tuffs RJ, Lemke D, Xu C, et al. 1996. *Astron. Astrophys.* 315:L149–52

van Loon JT, Bailey M, Tatton BL, et al. 2013. *Astron. Astrophys.* 550:A108

Vanzi L, Hunt LK, Thuan TX, Izotov YI. 2000. *Astron. Astrophys.* 363:493–506

Vega O, Bressan A, Panuzzo P, et al. 2010. *Ap. J.* 721:1090–104

Vermeij R, Peeters E, Tielens AGGM, van der Hulst JM. 2002. *Astron. Astrophys.* 382:1042–51

Viaene S, Baes M, Tamm A, et al. 2017. *Astron. Astrophys.* 599:A64

Viaene S, De Geyter G, Baes M, et al. 2015. *Astron. Astrophys.* 579:A103

Vidal-Madjar A, Andreani P, Cristiani S, et al. 1987. *Astron. Astrophys.* 177:L17–L20

Vogler A, Madden SC, Beck R, et al. 2005. *Astron. Astrophys.* 441:491–511

Walsh W, Beck R, Thuma G, et al. 2002. *Astron. Astrophys.* 388:7–28

Walter F, Cannon JM, Roussel H, et al. 2007. *Ap. J.* 661:102–14

Weingartner JC, Draine BT. 2001. *Ap. J. Suppl.* 134:263–81

Welty DE, Federman SR, Gredel R, Thorburn JA, Lambert DL. 2006. *Ap. J. Suppl.* 165:138–72

Welty DE, Lauroesch JT, Blades JC, Hobbs LM, York DG. 1997. *Ap. J.* 489:672–92

Welty DE, Ritchey AM, Dahlstrom JA, York DG. 2014. *Ap. J.* 792:106

Whelan DG, Lebouteiller V, Galliano F, et al. 2013. *Ap. J.* 771:16

White RE III, Keel WC. 1992. *Nature* 359:129–31

Witt AN, Vijh UP. 2004. Extended red emission. In *Astrophysics of Dust*, ed. AN Witt, GC Clayton, BT Draine, pp. 115–39. San Francisco: Astron. Soc. Pac.

Wood K, Whitney BA, Robitaille T, Draine BT. 2008. *Ap. J.* 688:1118–23

Wu R, Hogg DW, Moustakas J. 2011. *Ap. J.* 730:111

Wu R, Madden SC, Galliano F, et al. 2015. *Astron. Astrophys.* 575:A88

Wu Y, Charmandaris V, Huang J, Spinoglio L, Tommasin S. 2009. *Ap. J.* 701:658–76

Xilouris EM, Byun YI, Kylafis ND, Paleologou EV, Papamastorakis J. 1999. *Astron. Astrophys.* 344:868–78

Yamagishi M, Kaneda H, Ishihara D, et al. 2012. *Astron. Astrophys.* 541:A10

Yamagishi M, Kaneda H, Ishihara D, et al. 2015. *Ap. J.* 807:29

Yoshida M, Kawabata KS, Ohyama Y. 2011. *PASJ* 63:493–503

Ysard N, Köhler M, Jones A, et al. 2015. *Astron. Astrophys.* 577:A110

Zeegers ST, Costantini E, de Vries CP, et al. 2017. *Astron. Astrophys.* 599:A117

Zhukovska S. 2014. *Astron. Astrophys.* 562:A76

Zubko V, Dwek E, Arendt RG. 2004. *Ap. J. Suppl.* 152:211–49

Zubko VG, Laor A. 2000. *Ap. J. Suppl.* 128:245–69

Contents

Indexes

Errata

An online log of corrections to *Annual Review of Astronomy and Astrophysics* articles may
be found at http://www.annualreviews.org/errata/astro